Published in final edited form as:
Phys Med Biol. 2009 October 7; 54(19): R59–R97. doi:10.1088/0031-9155/54/19/R01.

Photoacoustic tomography and sensing in biomedicine

Changhui Li and **Lihong V. Wang**
Optical Imaging Laboratory, Department of Biomedical Engineering Washington University in St. Louis, St. Louis, MO 63130, USA

Lihong V. Wang: lhwang@biomed.wustl.edu

Abstract

Photoacoustics has been broadly studied in biomedicine, for both human and small animal tissues. Photoacoustics uniquely combines the absorption contrast of light or radio frequency waves with ultrasound resolution. Moreover, it is non-ionizing and non-invasive, and is the fastest growing new biomedical method, with clinical applications on the way. This article provides a brief review of recent developments in photoacoustics in biomedicine, from basic principles to applications. The emphasized areas include the new imaging modalities, hybrid detection methods, photoacoustic contrast agents, and the photoacoustic Doppler effect, as well as translational research topics.

1. Introduction

The photoacoustic (PA) effect, also called optoacoustic or thermoacoustic (TA) effect, refers to the generation of acoustic waves from an object being illuminated by pulsed or modulated electromagnetic (EM) radiation, including optical and radio frequency (RF) waves or microwaves. This effect was first reported by Alexander Graham Bell in 1880, who found that audio waves can be generated from objects illuminated by chopped sunlight [1]. However, research on the PA effect made little progress for about 80 years after its discovery, primarily due to the lack of appropriate light sources. It was not until the 1970s that photoacoustics regained interest, after L. B. Kruezer reported its application in detecting gas constituents by using a laser-induced PA effect [2]. Photoacoustics has since been widely implemented in physics, chemistry, biology, engineering, and medicine [3,4].

Although the applications of the PA effect in biomedicine began in the 1970s [5], progress was slow until the last decade of the 20th century, when many pioneering works demonstrated the PA effect in optically scattering media and biological tissue [6,7,8,9,10]. Photoacoustics in biomedicine combines the merits of optical and acoustical methods: sensitive optical absorption contrast and low acoustic scattering in soft tissue. Using safe illumination sources, the PA effect can be applied to *in vivo* biological tissues. In addition, optical absorption, including RF wave absorption, is highly related to molecular constitution and formation. Thus, PA signals contain functional and molecular information. The history of PA in biomedicine can be traced in SPIE proceedings [11,12,13,14,[15],16,17,18,19].

Although most high-resolution pure optical detection methods are capable of detecting optical absorption, they primarily depend on detecting the variation in the reflected light. They are generally much less sensitive to optical absorption than PA detection [20]. In addition, PA detection can also take advantage of the penetration of diffused light to detect signals from deeper regions.

A primary PA application in biomedicine is photoacoustic tomography (PAT). The past decade has seen fast developments in both theoretical reconstruction algorithms and innovative imaging techniques, and PAT has been implemented in imaging different tissues, from

centimeter-large breast tumors to several micrometer-large single red blood cells (RBC). PAT now provides structural, functional, and molecular imaging. In addition to imaging, the PA effect is also studied to monitor temperature, the chemical environment, and particle flow. As the technique has matured, translational research has become widely carried out.

PAT can be combined with current biomedical imaging and detection modalities, such as ultrasound and optical methods, providing multi-function detection. In addition, the hybrid methods are important for quantitative PAT.

Several review papers on the the PA effect in biomedicine have been published [21,22,20], covering fundamental principles, imaging modalities, and reconstruction algorithms. PA mechanism and applications are also discussed in book chapters [23,24]. In this article, brief introductions are given to those already covered topics, and we then focus on more recent developments. The article starts from the generation of PA signals in tissue, including the wave equation, biological optical absorbers, and the propagation of EM and acoustic waves in tissue. Then, we discuss current PAT modalities and image reconstruction algorithms. After that, we review PA contrast agents and molecular imaging, and discuss hybrid modalities, and other PA applications in biomedicine. Finally, the translational research is reviewed, followed by a summary. Throughout the article, representative recent works are illustrated.

2. The photoacoustic effect

2.1. Generation of PA signals

The fundamental principle of the PA effect can be simply described: An object absorbs EM radiation energy, the absorbed energy converts into heat, and the temperature of the object increases. As soon as the temperature increases, thermal expansion takes place, generating acoustic pressure in the medium. However, a steady thermal expansion (time invariant heating) does not generate acoustic waves, thus, the heating source is required to be time-variant.

Two types of EM sources generate PA signals: EM pulses and intensity–modulated continuous-wave (CW) EM waves. Although both types of source can be implemented in biomedicine, short EM pulses are mostly used because they provide a higher signal-to-noise ratio (SNR) and permit directly detecting the distance of the PA source through the time-resolved signals. In the following, the EM source always refers to a short EM pulse, being either optical or RF, unless otherwise noted.

2.1.1. EM absorption in biomedicine—All matters are composed of charged particles, such as nuclei, electrons, and ions. Even charge–neutral molecules or atoms contain equal amounts of oppositely charged particles. Electromagnetic waves interact with these charged systems by elastic scattering, Raman scattering, absorption, etc. In an absorption interaction, the absorbed energy can be transformed into heat or consumed in a chemical reaction (like photosynthesis). It can also be re-emitted as, for example, fluorescence. Only the portion that is turned into heat leads to the PA effect. In most cases of diagnostic PA detection, the heating effect dominates the absorption interaction. The fluorescence effect is important only when the radiation source is in the ultraviolet or violet (UV/V) spectrum [25], which is out of the source spectrum used in most of PA applications in biomedicine. Moreover, the radiation intensity used in PA detection is below the safety limit, guaranteeing no chemical reactions in the tissue. The absorption ability depends on the molecular constitution, ion density, environmental condition, EM wavelength, EM polarization, etc. Details of the absorption mechanism are out of the scope of this paper.

Although the absorption spectrum of most of living tissues present a continuous pattern, the absorption value can be highly sensitive to the wavelength, as shown in Fig. 1. Thus,

photoacoustics are intrinsically suited for spectroscopic detection. Typical biological absorbers include blood, melanosomes, water, etc.

The hemoglobin molecule is the primary absorber in the blood. There are two kinds of hemoglobin molecules in blood: oxygenated hemoglobin (HbO_2) and deoxygenated hemoglobin (Hb), which have different absorption characteristics. Fig. 1(a) shows the dependence of their molar extinction coefficients on the illumination wavelength. The blood in living tissues generally contains a mixture of Hb and HbO_2, thus, the absorption coefficient μ_a of the blood at position **r** can be calculated by [26]

$$\mu_a(\lambda, \mathbf{r}) = 2.303 \times [\varepsilon_{Hb}(\lambda)[\mathrm{Hb}](\mathbf{r}) + \varepsilon_{HbO_2}(\lambda)[\mathrm{HbO_2}](\mathbf{r})], \quad (1)$$

where λ is the wavelength, ε_{Hb} and ε_{HbO_2} are Hb and HbO_2 molar extinction coefficients ($cm^{-1}M^{-1}$), respectively, and [Hb] and [HbO_2] are molar concentrations of two kinds of hemoglobin (mol/L), respectively. Although the total hemoglobin concentration, [Hb]+[HbO_2], is relatively constant in the normal adult blood (typical value is 2.33×10^{-3} mol/L), the absorption coefficient of blood depends not only on the wavelength, but also on the ratio of concentrations between Hb and HbO_2. In physiology, the hemoglobin oxygen saturation (SO_2), defined by

$$SO_2 = \frac{[\mathrm{HbO_2}]}{[\mathrm{Hb}] + [\mathrm{HbO_2}]}, \quad (2)$$

describes the relative concentration of the two kinds of hemoglobin. Therefore, the artery blood and vein blood usually have different optical absorption coefficients due to their differences in SO_2.

Figure 1(b) provides the absorption coefficients of cutaneous melanosomes, blood and water [26, 27]. Here, we calculated the light absorption of blood by averaging the absorption coefficients of artery and vein bloods, with the assumption that the artery and vein bloods contain 95% and 65% of SO_2, respectively. Human body contains about 75% of water and 7% of blood. The melanosome is the most common pigment in tissue, especially in the skin. It contains light-absorbing molecules, called melanin. The concentration of melanin in the melanosome can vary up to 10 times, so does the absorption ability. The approximate spectral dependence of the absorption characteristic of melanosome in the skin is given by S. Jacques as [28]

$$\mu_a = 1.7 \times 10^{12} \times \lambda^{-3.48}, \quad (3)$$

where λ is in nm and μ_a is in cm^{-1}. Blood, melanosome and water play important roles in EM absorption by biological tissues.

In addition to endogenous absorbers in tissue, exogenous absorbers also exist, such as contrast agents, artificial implants, and foreign bodies from trauma. We will discuss the application of contrast agents in Section 5.

2.1.2. Wave equation—The EM pulse used to generate PA pressure wave usually has a pulse width, τ, so short that thermal diffusion can be neglected. This condition is called the thermal confinement condition [21,20], i.e.,

$$\tau<\tau_{th}=\frac{d_c^2}{4D_T}, \tag{4}$$

where τ_{th} is the thermal confinement threshold, d_c is the characteristic dimension (targeted spatial resolution), and D_T is the thermal diffusivity (~ 0.14 mm^2/s for tissue [29]). For instance, a 50 μm spatial resolution has a threshold τ_{th} ~ 4.5 ms. A typical laser source used in PAT has a pulse width of ~ 10 ns. Under this condition, PA pressure generated in an acoustically homogenous and non-viscous medium is described by [30,31]

$$\nabla^2 p(\mathbf{r},t)-\frac{1}{\upsilon_s^2}\frac{\partial^2}{\partial t^2}p(\mathbf{r},t)=-\frac{\beta}{C_p}\frac{\partial}{\partial t}H(\mathbf{r},t), \tag{5}$$

where $H(\mathbf{r}, t)$ is a heating function defined as the thermal energy converted at spatial position $\mathbf{r}$ and time t by the EM radiation per unit volume per unit time, C_p is the isobaric specific heat in J/(K · kg), β is the isobaric volume expansion coefficient in K^{-1}, υ_s is the acoustic speed ($\upsilon_s^2=1/\rho\kappa_s$, and κ_s is the adiabatic compressibility in Pa^{-1}).

The amount of generated heat by tissue is generally proportional to the strength of the radiation. Explicit expressions of the heating function for optical and RF illumination are:

$$H(\mathbf{r},t)=\begin{cases}\mu_a(\mathbf{r})\Phi(\mathbf{r},t) & \text{(for optical illumination)}\\ \sigma(\mathbf{r})<\mathbf{E}^2(\mathbf{r},t)> & \text{(for RF illumination).}\end{cases} \tag{6}$$

Here, μ_a and Φ are the absorption coefficient and the optical radiation fluence rate, respectively, and σ and $\mathbf{E}$ are the conductivity and the electrical field strength, respectively. $<\cdots>$ represents short-time averaging [32]. RF heating is also often denoted by the specific absorption rate (SAR), and the relationship between $H(\mathbf{r}, t)$ and SAR is

$$H(\mathbf{r},t)=\rho(\mathbf{r})\cdot \mathrm{SAR}(\mathbf{r},t). \tag{7}$$

In many cases, the EM pulse is so short that not only the thermal diffusion but also the volume expansion of the absorber during the illumination period is negligible. This condition is referred to as the acoustic stress confinement, i.e.,

$$\tau<\tau_{st}=\frac{d_c}{\upsilon_s}, \tag{8}$$

where τ_{st} is the stress confinement threshold, which is generally less than τ_{th}. Under both thermal and stress confinement conditions, heating time can be treated as a delta function, i.e., $H(\mathbf{r}, t) \approx A(\mathbf{r})\delta(t)$. Therefore, the initial pressure p_0 of the absorber at location $\mathbf{r}$ after absorbing EM energy can be calculated by [20]

$$\begin{aligned} p_0(\mathbf{r}) &= \frac{\beta}{\kappa_t\rho C_\upsilon}A(\mathbf{r})\\ &= \frac{\upsilon_s^2\beta}{C_p}A(\mathbf{r})\\ &= \Gamma A(\mathbf{r}), \end{aligned} \tag{9}$$

where κ_t is the isothermal compressibility, C_v is isochoric specific heat, $A(\mathbf{r})$ is the absorbed energy density (specific optical absorption) that is transformed into heat at location $\mathbf{r}$, and Γ is defined as the Grueneisen parameter (dimensionless). For soft tissue at room temperature, $\beta \sim 4 \times 10^{-4}\, K^{-1}$, $C_p \sim 4 \times 10^3$ J/kg · K, and $\upsilon_s \sim 1.5 \times 10^3$ m/s, thus $\Gamma \sim 0.25$. The Grueneisen coefficient changes with temperature. Thus, the PA technique can be used to monitor temperature [33].

Equation (9) can be used to estimate the initial pressure after a short EM pulse illumination. For instance, if a blood vessel is illuminated by a pulsed laser with a wavelength of 800 nm and at a fluence of 20 mJ/cm^2, with the known absorption coefficient at this wavelength ($\mu_a \sim 4.3\ \text{cm}^{-1}$), the heat deposition density $A \approx 9 \times 10^4$ J/m^3, leading to $p_0 \sim 2.2 \times 10^4$ Pa (200 mbar). However, the pressure arriving at the ultrasonic detector is generally much less than its initial value, which will be explained later.

2.2. Forward solution

The wave equation of the PA wave generation can be solved by using a Green function approach. The general Green function in an infinite homogenous and non-viscous medium satisfies

$$(\nabla^2 - \frac{1}{\upsilon_s^2}\frac{\partial^2}{\partial t^2})G(\mathbf{r}, t; \mathbf{r}', t') = -\delta(\mathbf{r} - \mathbf{r}')\delta(t - t'), \tag{10}$$

which can be solved as

$$G(\mathbf{r}, t; \mathbf{r}', t') = \frac{\delta(t - t' - |\mathbf{r} - \mathbf{r}'|/\upsilon_s)}{4\pi|\mathbf{r} - \mathbf{r}'|}. \tag{11}$$

With this Green function, the PA wave equation can be solved for p:

$$\begin{aligned} p(\mathbf{r}, t) &= \int dt' \int d\mathbf{r}' G(\mathbf{r}, t; \mathbf{r}', t') \frac{\beta}{C_p} \frac{\partial H(\mathbf{r}', t')}{\partial t'} \\ &= \frac{\beta}{4\pi C_p} \int d\mathbf{r}' \frac{1}{|\mathbf{r} - \mathbf{r}'|} \frac{\partial H(\mathbf{r}', t - \frac{|\mathbf{r} - \mathbf{r}'|}{\upsilon_s})}{\partial t} \\ &= \frac{\beta}{4\pi C_p} \frac{\partial}{\partial t} \int d\mathbf{r}' \frac{1}{|\mathbf{r} - \mathbf{r}'|} H(\mathbf{r}', t - \frac{|\mathbf{r} - \mathbf{r}'|}{\upsilon_s}). \end{aligned} \tag{12}$$

For a short EM pulse that satisfies the acoustic stress confinement, the heating process can be treated approximately as a Dirac delta function, i.e., $H(\mathbf{r}', t') \approx A(\mathbf{r}')\delta(t')$. Substituting it into Eq. (12) yields

$$\begin{aligned} p(\mathbf{r}, t) &= \frac{\beta}{4\pi C_p} \frac{\partial}{\partial t} \left[\frac{1}{\upsilon_s t} \int d\mathbf{r}' A(\mathbf{r}') \delta(t - \frac{|\mathbf{r} - \mathbf{r}'|}{\upsilon_s}) \right] \\ &= \frac{1}{4\pi \upsilon_s^2} \frac{\partial}{\partial t} \left[\frac{1}{\upsilon_s t} \int d\mathbf{r}' p_0(\mathbf{r}') \delta(t - \frac{|\mathbf{r} - \mathbf{r}'|}{\upsilon_s}) \right], \end{aligned} \tag{13}$$

where p_0 is the initial pressure defined in Eq. (9).

Equation (13) tells us that the detected pressure at spatial location $\mathbf{r}$ and time t comes from sources over a spherical shell centered at $\mathbf{r}$ with a radius of $\upsilon_s t$, as shown in Fig. 2(a). Figure 2(b) is a typical example of the PA wave from a spherical source, centered at $\mathbf{r}_s$ with radius a and spatially uniformly excited by a delta EM pulse. The spherical absorber produces initial

pressure $p_0(\mathbf{r}) = A_0 U(a - |\mathbf{r} - \mathbf{r}_s|)$, where A_0 is the amplitude of the initial pressure and $U(x)$ is the step function, with $U(x) = 1$ when $x \geq 0$, and $U(x) = 0$ when $x < 0$. The analytical solution for the acoustic pressure, at $\mathbf{r}_0$ and time t, emitted from this spherical source is

$$p(\mathbf{r}_0, t) = A_0 U(a - |R - \upsilon_s t|)(R - \upsilon_s t)/(2R), \tag{14}$$

where $R = |\mathbf{r}_0 - \mathbf{r}_s|$ [31]. Figure 2(b) plots the pressure wave detected at a distance of 20 mm from an uniform spherical source with a radius of 2.0 mm. The calculation assumes an acoustic speed of 1.5 mm/s and a unit initial pressure.

Here, we further use the example in Fig. 2(b) to address several characteristic properties of the pressure wave generated in PA effect. First, although the initial pressure is always positive, the pressure wave generally has both positive and negative amplitudes, i.e., a bipolar shape. Fig. 2(b) shows a typical “N-shape” PA profile. Second, the pressure value of the PA wave at the distance far from the source is approximately proportional to the size of the source object, but inversely proportional to the distance from the source object. The decay with distance explains why the detected pressure from a spherical source is much weaker than its initial pressure value, since the detection distance can be very large (up to the order of 100) compared with the PA source size. Third, temporal width of the PA signal from a single target is proportional to its size, in other words, the smaller object the more higher frequency components in the generated PA signal spectrum.

In addition to pressure, the velocity potential ϕ_υ is also frequently used, defined as follows,

$$\begin{aligned} \phi_\upsilon(\mathbf{r}, t) &= \int_0^t dt' p(\mathbf{r}, t') \\ &= \frac{\beta}{4\pi C_p} \int d\mathbf{r}' \frac{1}{|\mathbf{r} - \mathbf{r}'|} H(\mathbf{r}', t - \frac{|\mathbf{r} - \mathbf{r}'|}{\upsilon_s}). \end{aligned} \tag{15}$$

For a delta pulse, we have

$$\phi_\upsilon(\mathbf{r}, t) = \frac{\beta}{4\pi C_p \upsilon_s t} \int d\mathbf{r}' A(\mathbf{r}') \delta(t - \frac{|\mathbf{r} - \mathbf{r}'|}{\upsilon_s}). \tag{16}$$

If we define $L(\mathbf{r}, t) = \frac{4\pi C_p \upsilon_s t}{\beta} \phi(\mathbf{r}, t)$, then

$$L(\mathbf{r}, t) = \int d\mathbf{r}' A(\mathbf{r}') \delta(t - \frac{|\mathbf{r} - \mathbf{r}'|}{\upsilon_s}), \tag{17}$$

which is in fact an integral of the specific optical absorption over a spherical shell with radius $\upsilon_s t$. Mathematically, Eq. (17) represents the spherical Radon transformation. Thus, the corresponding reconstruction algorithm becomes an inverse spherical Radon transformation, as will be discussed in the next section.

2.3. Propagation of EM and ultrasonic waves in tissue

The generation of PA pressure is discussed in Section 2.1. The forward solution is provided for a homogenous and non-viscous medium, which is not the case in actual tissues. Now, we briefly describe how the EM radiation field reaches the PA source and how the PA wave propagates in the tissue before it is detected by the ultrasonic transducer.

As discussed before, two EM spectral regions are mostly used to generate PA waves: optical and RF waves. The propagations of these two EM waves in tissue are different. For light, the propagation is usually modeled by the radiative transfer equation (RTE) [24], involving the scattering coefficient μ_s (~ 100 cm^{-1} in scattering tissues), the absorption coefficient μ_a (cm^{-1}), and phase function. Another very useful parameter is the reduced scattering coefficient μ_s' (~ 10 cm^{-1} in scattering tissues). Although the RTE does not have exact analytical solutions generally, it can be solved by Monte Carlo simulations, or under the diffusion approximation [24]. Detailed discussions of light transport in clear and turbid media are given in [24]. Here, two useful equations of the fluence rate, within the ballistic regime and in the diffusive regime, with plane wave illumination are provided:

$$\begin{aligned}\Phi(z) &= \Phi_0 e^{-\mu_a z} (\text{in the ballistic regime})\\ \Phi(z) &\approx \Phi_0 e^{-\mu_{eff} z} (\text{in the diffusive regime}),\end{aligned} \tag{18}$$

where Φ_0 is the illumination fluence, z is the depth, and $\mu_{eff} = \sqrt{3\mu_a(\mu_a+\mu_s')}$. As seen in the second line of Eq. (18), light attenuation depends on both scattering coefficient (μ_s') and absorption coefficient (μ_a). Although μ_a is much smaller than μ_s' in scattering tissue, the wavelength dependence of μ_s' is significantly smoother compared to that of μ_a over the visible and NIR spectral region. Thus, the absorption by the tissue plays an important role for the variations in the illumination depth, and consequently the detection depth of PA detection. From Fig. 1, water, blood, and melanin all have high absorption in the UV/blue region, and water also has high absorption in the IR region. Therefore, the appropriate optical spectrum for PA technique to detect deeper than the ballistic light regime (~ 1 mm in the turbid tissue) is from ~ 500 nm to NIR.

Since wavelengths of RF waves (including microwaves) are comparable to the size of the illuminated tissue, such as the breast, the EM diffraction effect dominates the propagation. Unlike light propagation in tissue, RF propagation depends not only on the tissue's dielectric properties, but also on the RF polarization state, antenna design, and environmental conditions [34,35]. It is generally needed to numerically solve Maxwell's equations with boundary conditions [34]. Numerical solvers for Maxwell's equations include the finite-difference time-domain (FDTD) method [36,34], discrete dipole approximation (DDA) method [37], etc. RF diffraction not only affects the global distribution of the EM field inside the tissue, but also causes image distortion if the absorber size is comparable with the RF wavelength in tissue [32].

Unlike light, which suffers strong scattering during the propagation in tissue, acoustic waves have much lower (2~3 orders smaller) scattering coefficients. In most cases, the scattering of the acoustic waves can be ignored for PA wave propagation in soft tissue. In addition, the generated PA pressure is on the order of mbars, where the nonlinear effect can also be safely ignored. However, the attenuation of the acoustic wave can not be always ignored, especially at high frequencies, or in highly absorptive acoustic media, such as the skull. For soft tissue and frequencies used in ultrasound medical imaging, the attenuation coefficient can be estimated as −0.3 dB/cm·MHz, an averaged value suggested by the Federal Drug Administration (FDA) 501(k) [38]. The attenuation coefficient of high frequency ultrasound waves varies with tissue and the individual, and can be high as −3 dB/cm·MHz [39,40]. In addition, since ultrasound attenuation increases with frequency, tissue works as a low-pass filter for ultrasound, which reduces spatial resolution for deeper objects. Thus, not only the amplitude, but also the temoral profile of a PA pressure wave is changed by ultrasound

attenuation. In general, a higher resolution of the PAT system detects higher frequency ultrasound waves, leading to a shallower detection depth due to higher acoustic absorption.

Both ultrasound attenuation and EM absorption affect the PA detection depth. Compensations for the attenuations of EM and acoustic waves are important in quantitative PA studies. In addition, appropriately selecting radiation wavelength and acoustic detection bandwidth is also important for quantitative study of highly absorptive objects. For instance, Sivaramakrishnan *et al.* demonstrated that the quantitative study of blood SO_2 by photoacoustic microscopy requires that the ultrasonic transducer's center wavelength must be shorter than the light penetration depth in blood, if the diameter of the blood vessel is greater than the penetration depth [41].

Moreover, the acoustic speed may also vary with tissue. Although acoustic heterogeneity should be considered in PA studies, photoacoustics can tolerate it better than pure ultrasound detection can. The PA pressure travels only one-way, instead of round-trip.

2.4. Radiation safety

To guarantee safe PA application in living humans, the radiation strength of the EM illumination must follow the safety limits set by American National Standards Institute (ANSI) [42], Institute of Electrical and Electronics Engineers (IEEE) [43], and FDA [44].

RF heating is measured as SAR in units of W/kg. According to the IEEE standards, at frequencies between 100 kHz and 6 GHz in a controlled environment, i.e., where the person is aware of the potential for exposure, the maximum SAR must be less than 0.4 W/kg averaged over the whole body, and the spatial peak SAR must be below 8.0 W/kg averaged over any 1 g of tissue. The SARs are averaged over any 6 minute interval. The FDA standards are more relaxed than the IEEE counterparts.

The ANSI laser safety standards [42] depend on the optical wavelength, pulse duration, exposure duration, and exposure aperture. ANSI has standards for laser exposure to the eye and skin. However, only a few PA applications for the eye have been reported. Table 1 shows the the maximum permissible exposure (MPE) values for the skin in the visible and NIR spectra. This table presents the MPE for three exposure durations. The ANSI requirement states, "For repetitive-pulse lasers the MPEs for skin exposure are applied as follows: Exposure of the skin shall not exceed the MPE based upon a single-pulse exposure, and the average irradiance of the pulse train shall not exceed the MPE applicable for the total pulse train, duration T." [42]. Consider, for instance, a pulsed laser source that generates repeated pulses of 532 nm wavelength and 5-ns pulse width, which shine on the same location of the skin, with a 1.0-cm^2 illumination area, for more than 10 s. In this case, the safety standard requires not only that each single pulse energy must be less than the $MPE^{(1)}$, which dictates a value of 20 mJ. Also, the averaged power must be less than the $MPE^{(3)}$, which dictates a value of 200 mW. Therefore, the maximum pulse energy in this application is 20 mJ at 10 Hz repetition rate, but only 10 mJ at 20 Hz. By comparison, for the same condition where the wavelength is changed to 800 nm, the maximum pulse energies are 31.7 mJ at 10 Hz and 15.8 mJ at 20 Hz. In addition to long period exposure, photoacoustic microscopy now uses fast raster scanning techniques, in which the same location of skin is illuminated for less than 10 s. The safety limit for raster scanning laser in the 400–700 nm spectrum is derived according to $MPE^{(2)}$, as follows:

$$E \times \sqrt[4]{F} \leq 2.75 \times 10^2 \pi d^{5/4} (\Delta/N)^{3/4}, \tag{19}$$

where E is the pulse energy in mJ, F is the repetition rate in Hz, d denotes the diameter of the illumination spot in cm, Δ denotes the scanning step size in cm, and N is the number of pulses

at each spot. The laser safety standards for other spectra, such as ultraviolet spectrum, or for illumination in eyes, can also be found in ANSI documents [42].

2.5. Signal processing

Due to noise and the limited bandwidth of a PA detection system, the recorded PA signal is modified from its original pressure profile. Without signal precessing, the reconstruction images might suffer low SNR or low resolution. Signal processing includes denoising and deconvolution.

Random noise can be minimized by signal averaging from multiple data acquisitions, at the expense of data acquisition time. However, signal averaging time is also limited by physiological changes in the tissue, such as tissue movement due to breaths or heart beats. Thus, the averaged raw data can still contain significant noise. There are several ways to further reduce the noise level from the raw data, such as the use of “moving averaging” and frequency filtering. “Moving averaging” works like a low-pass filter: it is suitable for suppressing high frequency noises when the signal itself contains primarily low frequency components. Frequency filtering can substantially suppress the noise level if the noise spectrum has limited overlap with the real PA pressure profile spectrum. As mentioned, the spectrum of the PA signal depends on the size of the target. In many cases, PA targets have different sizes, and signals from multiple targets can be superposed, leading to a broadband PA signal. Thus, the “moving averaging” method can smear out sharp changes in the original signal, and the frequency filtering method can potentially discard useful frequency components overlapped with noise. Both drawbacks reduce the image quality.

Over the past several decades, the wavelet method has become an important tool in signal processing, including wavelet-based denoising [45,46]. Wavelet denoising optimally preserves the useful signal and substantially suppress the noise level. Unlike Fourier transformation, wavelet transformation decomposes the time-domain signal into a series of scalable modulated window functions (basis functions) with different coefficients. These wavelet window functions are derived from a single mother wavelet by translation and scaling. Since coefficients corresponding to the white random noise are relatively small, wavelet denoising is generally achieved by thresholding small values of coefficients and then performing inverse wavelet transformation. Although many wavelet-based denoising algorithms and various mother functions have been developed, their performance can differ significantly for a given data set and depend on the experience of the user, which leads to a more complicated data analysis. Thus, it is desirable to develop an algorithm suited for PA signal processing. For instance, since a typical PA profile has a bipolar “N” shape, an “N-shape” function would be a good candidate for the mother function [47]. More background about wavelets and their applications in signal processing can be found in many books and journal papers [48,45,49, 50,46]. Several researchers have already implemented wavelet denoising methods in PA signal processing [51,52,53,47].

In addition to the noise, the finite bandwidth of the detection system distorts the profile of the recorded signal from that of the arriving pressure wave on the detector’s surface. Directly using the raw data in the image reconstruction can result in both image distortion and non-physical negative reconstructed initial pressure values, although the latter can be caused by other reasons such as limited views as well. For an ideal point detector, the detected signal is the convolution of the acoustic pressure and the system impulse response,

$$p_d(\mathbf{r}, t) = p(\mathbf{r}, t) * d_\delta(t)\,, \tag{20}$$

where $p_d(\mathbf{r}, t)$ is the recorded signal by a point detector at location **r** and time *t*, "*" represents the temporal convolution operation, and $d_\delta(t)$ is the detection system's impulse response. Thus, in the frequency domain, the initial pressure can be derived as

$$\tilde{p}(\mathbf{r}, \omega) = \frac{\tilde{p}_d(\mathbf{r}, \omega)}{\tilde{d}_\delta(\omega)}. \tag{21}$$

Theoretically, the original PA pressure profile can be calculated by inversely Fourier transforming $\tilde{p}(\mathbf{r},\omega)$. However, Eq. (21) can not be directly used due to the presence of noise and the detection system's limited bandwidth; otherwise, the noise signal would be magnified. Practically, deconvolution employs the zero routine, Wiener deconvolution, and other techniques. Eq. (22) gives two sample formulas for Wiener deconvolution and zero routine.

$$\begin{aligned} \tilde{p}(\mathbf{r}, \omega) &= \left[\frac{\tilde{d}_\delta^*(\omega) |\tilde{p}_d(\mathbf{r},\omega)|^2}{|\tilde{d}_\delta(\omega)|^2 |\tilde{p}_d(\mathbf{r},\omega)|^2 + \sigma_n^2} \right] \tilde{p}_d(\mathbf{r}, \omega), \quad \text{(Wiener deconvolution)} \\ \tilde{p}(\mathbf{r}, \omega) &= \frac{\tilde{d}_\delta(\omega) \tilde{p}_d(\mathbf{r},\omega)}{\tilde{d}_\delta(\omega)^2 + \delta^2}, \quad \text{(zero routine)} \end{aligned} \tag{22}$$

where $\tilde{d}_\delta^*(\omega)$ is the complex conjugate of $\tilde{d}_\delta(\omega)$, and σ_n and δ are two small-value threshold parameters that represent the noise variance of the detection system. Deconvolution methods have been used in PA image reconstruction [54,55].

Up to now, we have discussed the generation and propagation of PA pressure waves in tissue, EM radiation safety, and data processing. In the following chapters, we will review PA applications in biomedicine, including imaging and sensing, as well as their translational research.

3. PAT modalities

Over the past decade, various innovative forms of PAT have been developed. Based on the methods used in forming PA images, we classify the major current PAT modalities into three categories:

- **i.** PA computed tomography (PACT) relies on the computed image reconstruction to obtain images.
- **ii.** PA microscopy (PAM) uses a positively focused ultrasonic transducer and detects the PA signal coming primarily from the focal zone of the transducer. Each detection gives a 1D image. Depending on the method used to determine the lateral resolution, there are two types of PAM: acoustic-resolution PAM (AR–PAM) and optical-resolution PAM (OR–PAM).
- **iii.** PAT using an acoustic lens system is analogous to an optical imaging system, except for replacing the optical lens with an acoustic lens. Acoustic pressures are measured on the imaging plane.

Each imaging type has its advantages and applications. In the following, we give brief introductions to each modality, as well as typical examples.

3.1. PACT

PA computed tomography is often simply called PAT. If the illumination source is RF, it also refers to thermoacoustic tomography (TAT). PACT is widely studied due to its flexibility. Various types of acoustic detectors are used, including single-element transducers, acoustic

arrays, integrated transducers (line or large plane), virtual point transducers (ring-based or high-NA-based transducers), etc.

The scanning single-element finite size flat transducer, due to its simplicity and high sensitivity, is widely used in PAT [56,57]. Although commercial flat transducers are available with high sensitivity, most of them have limited acquisition angles, limiting the field of view [58]. A partial solution is to add a negatively focused lens over the flat transducer to achieve a wider acquisition angle [58].

Instead of using transducers made of piezoelectric materials, optical methods can be used to provide high sensitivity acoustic detection at high frequencies [59,60]. Zhang *et al.* developed an imaging system based on a planar Fabry-Perot film sensing interferometer (FPI) [59], as shown in Fig. 3. The arrival of acoustic pressure modulates the optical thickness of the film, changing the reflectivity of the Fabry-Perot mirror. A focused CW laser beam is shone on the film. The variation in the reflected light intensity is converted to pressure, measuring PA pressure at the focal spot. Scanning the focused laser over the film is equivalent to scanning a single-element transducer with an active area the size of the focal spot. Because the film is transparent to the PA illumination light, this imaging system is well suited for reflection mode detection.

In addition to scanning transducers that are much smaller than the region of interest, large planar and line detectors have also been studied. A large planar detector can be a piezoelectric plate much larger than the object to be imaged [61]. A line detector can be an optical fiber-based Fabry–Perot interferometer or a Mach–Zehnder interferometer [62]. Fig. 4 shows the setup for a line detector by using a Mach–Zehnder interferometer developed by Paltauf *et al.* [62], where the laser beam splits into one reference beam (away from the sample) and one signal beam (closer to the sample). The signal beam serves as the line ultrasonic detector. PA pressure waves slightly change the refractive index of water along the beam and the optical path, causing variation in the detected signal. From the variation, the integral of pressure along the line detector can be inversely obtained. Mathematically, under certain detection geometries, both large planar and line detectors can use the inverse Radon transformation to achieve exact image reconstruction.

Scanning a single transducer over the object can be time-consuming, thus an acoustic array is desirable. The array in a commercial ultrasound imaging system has been used to detect PA signals [63,64]. Some also added optical fibers on the acoustic array to deliver light, forming a hand-held PAT system [65]. In addition to these commercial arrays, array systems specially designed for PAT have also been developed. Zemp *et al.* presented a high frequency piezoelectric transducer array system for PAT [66,67]. This system has 48 elements with a center frequency at 30 MHz, providing a B-scan acquisition rate of 50 frames/s. High resolution has been also achieved. Gamelin *et al.* also developed a PAT system with a 5-cm diameter full-ring array having 512 elements with a center frequency at 5 MHz [68], each cylindrically focused.

3.1.1. Reconstruction algorithms—Both the imaging speed and image quality of PAT rely on the reconstruction algorithms. We present a brief introduction to reconstruction algorithms because details are available in other literatures [21,69]. Only the delta EM pulse illumination is considered because the pressure wave generated using a finite width EM pulse corresponds to the convolution of the pulse profile with the pressure wave generated by a delta EM pulse [21].

If the medium is acoustically homogenous, non-dispersive and nonviscous, reconstructing the initial pressure in the source from data collected by scanning point detectors is called the inverse

spherical Radon transformation, which is discussed in [21,22]. Finch *et al.* [70] and Kunyansky [71] both derived exact reconstruction formulations for spherical detection surface based on the inverse spherical Radon transformation. Kostli *et al.* derived an exact reconstruction algorithm for planar detection [72]. Xu and Xu *et al.* provided three exact reconstruction formulas, based on the mathematical techniques used for ultrasonic reflectivity imaging [73], for spherical, cylindrical, and planar detection surfaces [74,75,76]. Later on, a universal reconstruction formulation for these three geometries was also provided by Xu and Wang. [77,78], whose time-domain formulation is expressed as

$$p_0^{(b)}(\mathbf{r})=\frac{1}{\Omega_0}\int_s d\Omega\left[2p(\mathbf{r}_d,t)-2t\frac{\partial p(\mathbf{r}_d,t)}{\partial t}\right]\Big|_{t=|\mathbf{r}_d-\mathbf{r}|/v_s}, \tag{23}$$

where $d\Omega=dS/|\mathbf{r}-\mathbf{r_d}|^2\cdot[\mathbf{n_d^s}\cdot(\mathbf{r}-\mathbf{r_d})/|\mathbf{r}-\mathbf{r_d}|]$ is the infinitesimal solid angle at $\mathbf{r}_d$ with respect to the reconstruction point $\mathbf{r}$, and $\Omega_0=\int_s d\Omega$. For spherical and cylindrical detection geometries, $\Omega_0=4\pi$; for a planar detection geometry, $\Omega=2\pi$. Recently, Kunyansky provided an exact series solution solving the inversion of the spherical Radon transformation for any close detection surfaces which have explicit Dirichlet Laplacian eigenfunctions [79]. His work extends the exact analytical solutions available for more detection surfaces, including cubes, spheres, ellipsoids, etc. Up to now, there have been no exact analytical solutions valid for arbitrary detection surfaces except those aforementioned. Moreover, Burgholzer *et al.* presented an exact numerical reconstruction algorithm over an arbitrary surface [80], based on the time-reversal concept [81]. Because an ideal point detector never exists in practice, Xu *et al.* discussed the effects of the transducer's finite aperture and finite bandwidth on spatial resolution [82].

Using integrated large detectors of planar and line shapes can take advantage of the existing inverse Radon transformation to reconstruct PA image, as discussed in [83,84,62]. However, exact reconstructions are also only valid for specific scanning geometries: the large planar detector scans tangentially over a sphere that encloses the object; and the line detector scans perpendicularly around a circle or along an infinite long line.

Exact reconstruction algorithms require either enclosed detection surfaces (such as an sphere), or unbounded open surfaces (such as an infinite plane or an cylinder), which are generally impossible in practice. Many approximate reconstruction algorithms have been provided in both frequency-domain and time-domain formulations, and they are practically implemented in PAT. The most simple algorithm is delay and sum (also called synthetic aperture), which is borrowed from ultrasound imaging. Delay and sum is a simple back-projection algorithm, projecting time-domain original PA signals back into the imaging region over spherical shells centered at each detection position and summing them together. In the approximation that the object is located near the scanning center and far from the detector, filtered back-projection reconstruction algorithms have been derived based on the inverse Radon transformation [85]. Approximate algorithms have been also derived from the rigorous analytical reconstruction algorithms; for example, one can neglect the first term in the bracket of Eq. (23) if the source-detector distance is much greater than the interested acoustic wavelengths [77]. More detailed discussion can be found in [21].

In comparison to the temporal frequency, the frequency-domain reconstruction can be implemented more efficiently by using *k*-space methods for a planar and a linear scanning geometry [72,86,87]. Zhang *et al.* used this reconstruction method and obtained high quality images [59].

In practical *in vivo* PA imaging, both the PA detection area and the number of PA measurements are limited, which results in incomplete data. As a result, image artifacts are generated by using the previously mentioned analytical reconstruction algorithms. The artifacts can become significant when PA measurement locations are sparsely distributed. Iterative reconstruction methods can reduce artifacts and increase the image quality [88], at the expense of reconstruction time. In addition, real tissues might be acoustically heterogeneous, so assuming an uniform acoustic speed in such tissues will degenerate the resolution. An extreme case is the reconstruction of PA sources in the brain from detected signals over a thick skull, where the back-projection method with an uniform speed assumption generates severe artifacts [89]. Therefore, numerical iterative reconstruction has gained more and more interest. Phantom simulations and experiments have demonstrated the iterative method can significantly improve the image quality [90]. Moreover, the iterative algorithm can also use prior knowledge to increase the reconstruction speed and accuracy, as well as a smaller number of measurements. For instance, if the PA image is known to be "sparse" with prior knowledge, Provost and Lesage implemented the so-called compressed sensing (CS) iterative method [91], which was initially developed for magnetic resonance imaging (MRI), in PAT [92]. They demonstrated that the CS method makes it possible to dramatically reduce the number of PA measurements needed for a given PA image quality. Another advantage of the iterative method is that it can combine the acoustic wave equation and the radiative transfer equation (RTE) to achieve quantitative PA reconstruction [93,94].

3.2. PAM

Unlike PACT, which depends on reconstruction algorithms to form images, PA microscopy, by using a positively focused ultrasonic transducer, detects PA pressure waves coming primarily from the focal zone [23]. Although the axial resolution is derived from the time-resolved detection, the lateral resolution can be determined either by acoustic focusing or optical focusing.

3.2.1. AR–PAM—Optical focusing becomes extremely difficult or impossible beyond the ballistic regime, where multiple scattering dominate the light propagation in tissue. Thus, pure optical high resolution imaging methods are limited within the ballistic or quasi-ballistic regime, which is ~ 1 mm below the skin.

Because acoustic scattering is small compared to optical scattering, focusing acoustic waves is easier in optically scattering biological tissues. AR–PAM uses a positively focused ultrasonic detector, which substantially suppresses signals generated outside the focal zone. Based on this method, for PA sources within the focal zone, AR–PAM can image deeply into the diffusive regime, with high lateral resolution of the acoustic focal width. In addition, the axial resolution can be derived from the time-resolved signal, with the resolution determined by the detector's bandwidth. Thus, detection with each laser pulse can provide a 1D image. By scanning the transducer over 1D and 2D regions, 2D B-scan and 3D images can be obtained.

Based on the relative position of the illumination head and ultrasonic detection head to the tissue, AR–PAM can work in both reflection mode, where these two heads are on the same side of the tissue, and transmission mode, where they are on opposite sides. Practically, reflection mode is more convenient for *in vivo* imaging. In reflection mode AR–PAM, bright field illumination could suffer from strong acoustic reverberations due to strong absorption near the surface, where considerable melanin may exist. The strong PA pressure waves generated by these strong absorbers can reverberate inside the detection system, such as the acoustic lens used in the focused transducer, and thus overshadow later arriving weak PA signals. In 2005, Maslov *et al.* introduced dark-field confocal AR–PAM [95], a design which mitigates the problem. Dark–field AR–PAM can achieve 45 μm lateral resolution and 3 mm

imaging depth at 50 MHz ultrasonic frequency, providing a powerful imaging tool for subcutaneous tissues. A typical image acquired by dark–field AR–PAM is shown in Fig. 5, where a melanoma in a mouse was imaged *in vivo*. Later on, Song and Wang. developed another version of AR–PAM [96], which uses a lower frequency transducer to image deeper at reduced resolution. The imaging depth can reach several centimeters, useful for imaging internal organs.

The image quality within the adjacent out-of-focus region can be improved by using a synthetic-aperture focusing technique (SAFT) plus coherent factor (CF) weighting. Both methods have been previously used in ultrasound imaging. Li introduced SAFT + CF into PAM data processing, using a virtual point concept [98]. SAFT treats the transducer's focal point as a virtual point detector, and the CF weighting significantly increases the lateral resolution.

3.2.2. OR–PAM—According to the scalability of PAT, higher resolution AR–PAM can be achieved by using higher center frequency ultrasonic transducers. However, high frequency acoustic waves are attenuated severely in tissue [39], which can limit the imaging depth of AR–PAM even shallower than that of pure optical imaging methods. For instance, to image a 5-μm capillary, AR–PAM needs to use a transducer with a center frequency of about 300 MHz. However, the attenuation of an acoustic wave at 300 MHz is about – 80 dB/mm in tissue, and the detectable PA signal only travel less than 500 μm.

Within the ballistic regime, light focusing is feasible. Instead of using higher frequency transducers, OR–PAM uses optical focusing to provide the lateral resolution, while the axial resolution is still derived from the time-resolved PA signals. Maslov *et al.* developed the first OR–PAM system [99]. Their system has already achieved 5 μm lateral resolution and 15 μm axial resolution. The detection head of the system is shown in Fig. 6(a), and small capillaries in the mouse ear have been successfully imaged *in vivo*, as shown in Fig. 6(b). The lateral resolution of OR–PAM can be further increased by using a higher NA objective lens or a shorter illumination laser wavelength.

Unlike AR–PAM, which takes advantage of diffused light to image deeper tissues, OR–PAM has a similar imaging depth as high resolution pure optical imaging methods. But OR–PAM has a much higher image contrast in imaging the microvasculature or other strong light absorbers in tissue than these optical methods. The extremely small light absorption in surrounding tissues provides OR–PAM with an almost dark background. However, optical scatterers, such as different cells, exist almost everywhere within tissue. In order to have a high quality microvasculature image, pure optical imaging methods usually use fluorescence from exogenous dyes.

The high optical scattering in the skin significantly limits the imaging depth of OR–PAM. However, eyes are potential targets for OR–PAM, owing to their low light scattering. Kong *et al.* developed another OR–PAM with a long focal length [100], targeting applications in imaging eye tissues, such as the retina.

The idea of using optical focusing to detect signals from regions smaller than the acoustic resolution was also used by Zharov *et al.* in their PA flow cytometry (PAFC)[101]. They detected signals from single cells passing through the optical focal zone. Details of PAFC are described in 7.3.

3.3. PAT based on an acoustic lens system

Analogous to imaging by using an optical lens, imaging can also be achieved by using an acoustic lens. There are several advantages to PAT using the acoustic lens: (a) no image reconstruction is needed; (b) the transducer array can be put at the imaging plane to achieve

real-time detection; and (c) the acoustic lens can project the the initial PA pressure distribution from the optically turbid medium to an optically clear medium, where optical detection can be applied.

Niederhauser *et al.* were the first to present a PAT system based on a 4f acoustic lens system with optical detection [102], which used a 30 ns flash light as the illumination source, and detected the signal by a CCD. Later on, Chen *et al.* [103] used a linear ultrasonic array placed at the image plane of a 4f lens to acquire the PA image. The array has 64 elements centered at 1.0 MHz, and the system has a lateral resolution ~ 3 mm. Image quality and resolution are limited by the array, the acoustic lens aperture, and lens aberrations.

Overall, we have discussed three types of PAT: PACT, PAM, and acoustic-lens-based PAT. Since just a few works have reported on the last type, here we will compare only the first two types. PACT is the most versatile PA imaging modality. Various detectors and system designs have been developed. Since each ultrasonic detector used in PACT detects PA signals coming from a wide region, PACT is especially suitable to image a large area. In addition, by using ultrasonic arrays, PACT can provide realtime imaging. The image quality of PACT is highly affected by the detection geometry and reconstruction algorithms. In comparison, PAM provides high resolution imaging primarily for targets within the acoustic focal zone. Although PACT can image the same region with the same resolution as PAM by using a high frequency array, PAM has no discretization artifacts, whereas PACT generally has reconstruction artifacts. In addition, PAM is currently implemented with single-element ultrasonic transducers and therefore is much less expensive than array-based PACT. However, the imaging speed of PAM is restricted by the mechanical scanning speed and the laser repetition rate, which makes it challenging for PAM to image a large area in real time.

The classification of three types of imaging modalities in this chapter is by no means exclusive. There are various designs of acoustic detectors, as well as various detection methods. For example, Kolkman *et al.* presented a double-ring acoustic sensor [104], which, like PAM, acquires 1D images at each detection, but also uses a computational algorithm to correlate the signals detected by the two ring detectors. As another example, SAFT used in PAM also reconstructs the value of a single pixel from multiple PA measurements.

In addition to previously discussed PAT methods that use short EM pulses as the illumination source, intensity modulated continuous wave (CW) lasers can also serve as the illumination sources. For example, Telenkov and Mandelis presented a frequency-domain version of PAM [105], shown in Fig. 7. In their setup, the laser power is modulated by linearly chirping the frequency. Detected PA signals are processed by using either correlation processing or heterodyne mixing. The frequency-domain modulation provides the same axial resolution as that of the pulsed source, with the same bandwidth. With a sweep bandwidth of 4 MHz, this system can achieve axial resolution less than 1.0 mm, and the lateral resolution is determined by the ultrasound focusing. Recently, Maslov and Wang [106] demonstrated another method, modulating the laser power at a fixed frequency. The advantage for single frequency modulation PAM compared with frequency–swept PAM is that the SNR can be increased by using a narrow band transducer, which has a resonance frequency the same as the modulation frequency. However, without frequency sweeping, no axial resolution for a planar feature is provided. The advantages of using intensity-modulated CW lasers include inexpensive illumination sources and narrow-band detection. More studies in this direction are expected.

4. Functional imaging and PA spectroscopy

PAT is based on the absorption properties of the target. Since optical or RF absorption in tissue is highly sensitive to biological activities, such as metabolism, PAT is suitable for functional imaging. Moreover, by using multiple wavelengths, spectroscopic PAT can reveal more

functional information about the tissue. Although there are many potential absorbers as described in Sec. 2.1.1, most PA functional imaging research targets the blood vessel.

In 2003, Wang *et al.* demonstrated that PAT can image cortical neural activities during whisker stimulation of a rat by detecting changes in PA signals from the cortex vasculature [56]. In the same work, they also demonstrated the detection of blood volume changes from hyperoxia to hypoxia in a rat cerebral cortex. Yang *et al.* studied changes in mouse cerebral cortex blood flow induced by either carotid artery occlusion or drug stimulation by acetazolamide (ACZ) [107]. Zemp *et al.* reported real-time imaging of murine cardiovascular dynamics by PAT [108].

4.1. PA spectroscopy

Based on the optical absorption contrast, PA spectroscopy detects the spectrally dependent absorption characteristics of different tissues. An important PA functional imaging application is SO_2 imaging using spectroscopic PAT. SO_2 is a very important physiological parameter which is closely related to the local metabolic rate. For instance, the region of a tumor generally has an abnormally low SO_2 value. Thus, measuring SO_2 distribution helps to detect tumors. If the Grueneisen parameter is constant and the light penetration depth is greater than the vessel diameter, the PA signal amplitude from the same vessel is proportional to the product of the blood absorption coefficient and the local fluence $\phi(\lambda, \mathbf{r})$. The blood absorption coefficient also depends on [Hb] and [HbO_2], as shown in Eq. (1). Spectroscopic PAT, using multiple wavelengths ($\lambda_1, \lambda_2 \cdots, \lambda_n$), forms images of the distribution of EM energy deposition ($A(\lambda, \mathbf{r})$). If the local fluence is known, the [Hb] and [HbO_2] of a blood vessel at position $\mathbf{r}$ can be calculated by using least-squares fitting, which is described in [109], as follows.

$$\begin{bmatrix} [\mathrm{Hb}] \\ [\mathrm{HbO_2}] \end{bmatrix}_{(\mathbf{r})} = (M^T M)^{-1} M^T K(\mathbf{r}), \tag{24}$$

where

$$M = \begin{bmatrix} \varepsilon_{Hb}(\lambda_1) & \varepsilon_{HbO_2}(\lambda_1) \\ \vdots & \vdots \\ \varepsilon_{Hb}(\lambda_n) & \varepsilon_{HbO_2}(\lambda_n) \end{bmatrix}, \quad K(\mathbf{r}) = \begin{bmatrix} A(\lambda_1, \mathbf{r})/\phi(\lambda_1, \mathbf{r}) \\ \vdots \\ A(\lambda_n, \mathbf{r})/\phi(\lambda_n, \mathbf{r}) \end{bmatrix}. \tag{25}$$

Finally, SO_2 is computed by substituting the calculated [Hb] and [HbO_2] into Eq. (2).

Without calibrating the local spectrally dependent fluence, $\phi(\lambda, \mathbf{r})$, SO_2 can be estimated approximately. For instance, Kruger *et al.* imaged small animals at multiple NIR wavelengths to calculate the blood oxygenation levels in different types of tissues [110]. Stantz *et al.* also studied the SO_2 distribution inside a tumor [111]. In addition, except for the absolute value, the relative differences in SO_2 between nearby vessels can be reliably calculated without local fluence compensation, as discussed in [112].

Accurate quantitative studies of the absolute SO_2 generally requires the information about local fluence [112]. It is still challenging to obtain spectrally dependent fluence *in vivo*. There are no universal optical parameters valid for all tissues, thus the local fluence varies from case to case. Invasive methods include putting a spectrally neutral or spectrally calibrated optical absorber under the skin close to the field of interest [109,112]. By measuring the amplitude of the generated PA signal from this absorber at multiple wavelengths, spectrally dependent fluence can be estimated relatively to each other. Several *in vivo* functional imaging studies

that have used this approach have been undertaken. For example, by using multiple wavelengths in PACT, Li *et al.* studied oxygen saturation changes due to the tumor in the cerebral cortex of a nude mouse [113]. Wang *et al.* studied the SO_2 changes in a rat cerebral cortex [114]. As mentioned, PAM currently provides higher resolution than PACT. Zhang *et al.* demonstrated functional imaging by using multiple wavelengths in a dark-field PAM system [115,97,109]. Fig. (8) presents an *in vivo* SO_2 image of subcutaneous blood vessels of a rat, showing hypoxia, normoxia, and hyperoxia states. Furthermore, OR-PAM can study SO_2 at the capillary level.

Noninvasive methods generally requires the solution of the coupled radiative transfer equation (RTE) and PA wave equation at multiple wavelengths, which is normally solved by iterative algorithms [94,116]. Prior knowledge and assumptions are usually required to ensure a unique solution. For example, Laufer *et al.* presented a model-based inversion scheme to recover the concentration of tissue chromophores. They used a finite-element method to solve the RTE, and the prior knowledge in their model includes the spectrally dependent molar absorption coefficients of lipid, water, and the anisotropy parameter of the tissue scattering. Recently, Cox *et al.* reviewed different iterative methods that are implemented in PAT [117].

All previously mentioned quantitative PA detection methods are based on the linear relationship between the amplitudes of the fluence and the PA pressure. However, quantitative detection can also be achieved by using the non-linear relationship between the EM energy deposition and the absorption coefficient. For a simple example, if a pencil beam shines perpendicularly to the blood vessel surface with a fluence of $\Phi_0(\lambda)$, the EM energy deposition along the beam in the vessel is approximately

$$A(z)=\mu_a(\lambda)\Phi_0(\lambda)e^{-\mu_a(\lambda)z}, \tag{26}$$

where $\mu_a(\lambda)$ is the spectrally dependent absorption coefficient, and z is the traveling depth of the pencil beam. The exponential-decay term in Eq. (26) presents a nonlinear dependence of $A(z)$ on $\mu_a(\lambda)$. The absorption coefficient can be derived from either the reconstructed $A(z)$ or the PA pressure profile according to Eq. 13. This method requires the prior knowledge of the geometry and illumination condition of the absorber. The geometry can be derived from the PA detection or from the prior knowledge. Although the illumination condition can be noninvasively obtained from the solution of RTE as described before, it can be well estimated in some cases. For instance, when a small absorber deeply lies in the diffused light region, the illumination over it is almost uniform. This method was used by Petrov *et al.*, who monitored SO_2 changes in the human large internal jugular vein (IJV), which has a diameter of about 10 – 20 mm, by using three different wavelengths [118]. It is also described by Laufer *et al.* in their *in vitro* measurements of SO_2 [119]. However, it is challenging to apply this method to measuring SO_2 in small blood vessels that cannot be resolved.

Many normal and abnormal tissues have spectrally dependent EM absorption characteristics. For instance, Sethuraman *et al.* used multiple wavelengths to target lipids in their intravascular photoacoustic imaging system [120]. More research is expected in exploring different natural targets for PA spectroscopic biomedical detection. In addition, PA spectroscopic detection are widely used to detect various contrast agents, as discussed in Section 5.

5. PA contrast agents and molecular imaging

5.1. PA contrast agents

A PA signal is sensitive to the optical absorption of the target, thus optical contrast with high absorption can be used to increase the sensitivity and specificity. Different contrast agents,

including dyes and nanoparticles [121,122,123,124,125,126], have been studied. As we have discussed, NIR light sources are generally used for PA to detect deep in tissue, thus, contrast agents with high absorption in the NIR spectral region are highly desirable. In practical applications, the contrast agent can be administered into circulation systems, including blood and lymph circulations, or it can be directly injected at the tissue area of interest.

Contrast agents in the circulation of blood or lymph can increase the PA signal. A typical example is indocyanine green (ICG), a dye approved by FDA. ICG has high absorption in the NIR spectral region, and it has already been proved to increase the PA signal when it is injected in blood vessels [125]. Most recently, methyline blue was used as the contrast agent to detect the sentinel lymph node (SLN) [127], as seen in Fig. 9. The advantage of using dyes is that many dyes are non-toxic. However, dyes, without binding to other chemicals, often suffer from a short circulation time, limiting their applications in long-term PA monitoring.

Compared with dyes, nanoparticles possess a high and tunable absorption spectrum, and longer circulation time. The absorption peak is tunable by changing the shape and size of the particle. In addition, nanoparticles can be used to target certain diseases by bio-conjugating them with proteins, such as antibodies. Recently, Zerda *et al.* presented carbon nanotubes as a PA contrast agent [128]. In their study, single-walled carbon nanotubes, 1–2 nm in diameter and 50–300 nm in length, were conjugated with cyclic Arg–Gly–Asp (RGD) peptides to target mice bearing tumors. The PA increase of tumor by the bio-conjugated carbon nanotubes is eight-fold higher than that of the pure carbon nanotubes.

Among different nanoparticles, gold nanoparticles are favored in optical imaging due to their exceptional optical properties in the visible and NIR spectral ranges, including scattering, absorption and photoluminescence. Three types gold nanoparticles have been studied as PA contrast agents: nanorods [129,130,131,132], nanoshells [124] and nanocages [126]. Even without bio-conjugation, small gold nanoparticles (60–400 nm diameter) tend to accumulate in the tumor site due to the enhanced vascular permeability and retention caused by tumor. However, potential toxicity limits gold nanoparticles' *in vivo* applications. So far, none of the gold nanoparticles have been approved by FDA.

Most PA contrast agents are designed for absorbing laser, especially in the NIR spectral range. However, RF contrast agents are also desirable due to the superior penetration depth of RF in the body. Recently, researchers have begun to study the RF contrast agents. Nie *et al* did a preliminary study on the TAT contrast agent by using magnetic microspheres made of carbonyl iron [133]. Pramanik *et al* also presented a dual-functional contrast agent, made of the single wall carbon nanotube (SWNT), working in both optical and RF regimes [134]. We expect more new developments in this direction.

5.2. PA molecular imaging

By using PA contrast agents, PA molecular imaging can be achieved based on two major mechanisms: (a) Certain contrast agents change their optical or RF absorption properties triggered by changes in the molecular level; (b) Contrast agents with specific absorption spectra are bio-conjugated with certain proteins, targeting specific molecules.

Using the first mechanism, Li *et al.* imaged the expression of lacZ gene [135] by employing a sensitive chromogenic assay, 5-bromo-4-chloro-3-indolyl-β-D-galactoside (X-gal), which is optically transparent before the lacZ expression and turns dark blue after the expression. With a red illumination source ($\lambda = 650$ nm), the PA image clearly depicted the lacZ expression area.

The second molecular imaging mechanism, bio-conjugation, has also been used. Li *et al.* imaged the human U87 glioblastoma tumor, which was implanted stereotactically in a young

adult immunocompromised nude mouse, with a bio-conjugated dye called IRDye800 [113]. Zerda *et al.* used bio-conjugated carbon nanotubes to target mice tumour [128]. Gold nanoparticles, conjugated with antibodies, have also been used to image different cancers, as described previously.

6. Hybrid method

PAT does not replace any current biomedical imaging methods, however, it complements current methods. Because PAT combines optics and ultrasound, integrating PAT with either optical or ultrasound imaging methods is of interest.

Since they have already been equipped ultrasonic detectors, PAT systems can be made to acquire ultrasonic images in pulse-echo mode. Therefore, PAT can potentially provide not only PA images of endogenous absorbers, such as small blood vessels, but also ultrasound images of mechanical structures, indicating the boundaries of organs. As mentioned, commercial ultrasound detectors have been applied in PAT, such as hand-held arrays, as the PA detector while optical fibers are used to deliver light. A typical setup, used by Niederhauser *et al.* [65], is shown in Fig. 10, which used a 64-element commercial ultrasound array. This system can image several millimeters below the skin with 0.4 mm and 0.3 mm lateral and axial resolutions, respectively. Sethuraman *et al.* [136] used a high-frequency intravascular ultrasound (IVUS) imaging catheter to acquire intravascular PA (IVPA) images. This IVPA is intended to detect atherosclerosis. However, their system uses an external illumination source, which limits the application. A prototype photoacoustic endoscope system with integrated light delivery was recently developed by Yang *et al.* [137]. *Ex vivo* and *in situ* experiments demonstrated that this PA endoscope, working at 42 MHz ultrasonic center frequency, has a 3 mm imaging depth. Depending on the distance of the target, the radial and transverse resolutions are about 50–100 μm and 200–600 μm, respectively.

PAT and diffuse optical imaging also form a synergistic hybrid imaging modality. Although PAT can image into the diffused light region with high resolution, its signal is proportional to the local fluence, as in Eq. (9), so the quantitative imaging of tissue absorption requires information about the fluence value. Diffuse optical imaging, like diffuse optical tomography (DOT), can retrieve the fluence distribution but with low resolution of small absorbers. Thus, PAT can accurately provide the location and shape of the absorber to be used in DOT reconstruction, and DOT can provide local fluence information for PAT. Numerical iterations by PAT and DOT have the potential to provide a 3D image containing both absorption and scattering distribution information. Similarly, PAT also helps fluorescence molecular imaging (FMI) by providing the background absorption map, as done by Razansky and Ntziachristos [138].

With the emergence of high resolution OR–PAM, PAT has the potential to combine with other high resolution optical imaging methods. For instance, by combining OR–PAM with OCT or confocal microscopy, both light scattering and absorption characteristics of the target at high resolution can be achieved.

7. Other photoacoustic sensing

We have discussed PA applications in imaging vasculature structures, melanoma, and other cancerous diseases. PA detection can also be used to sense or image temperature change, cell identity, chemical environmental changes, particle flow velocity, etc.

7.1. Temperature monitoring

Real-time monitoring of temperature increase is important not only for the safety and efficiency of thermal therapy, but also for studying biological activities in tissue, such as the metabolic rate. Current methods to measure temperature *in vivo* include invasive thermocouples, and non-invasive methods, such as infrared thermography [139], ultrasound imaging [140,141], and magnetic resonance imaging (MRI) [142,143]. Although infrared thermography can give high sensitivity and realtime detection, it provides only superficial temperature measurement. Ultrasound can measure deep into tissue, but it has relatively low sensitivity and accuracy. MRI has high sensitivity, but it has poor temporal resolution, which limits its application in real time monitoring.

Temperature measurement based on the PA effect has the potential to be a non-invasive high sensitivity method for real time monitor of deep tissue and *in vivo*. As discussed in Sec 2.1.2, the PA pressure is proportional to the Grueneisen parameter Γ, which depends on the temperature. Thus, once the relation between the Grueneisen parameter and the temperature is known, temperature can be derived from the PA pressure amplitude. Although this relation can be complex, an approximately linear empirical equation describes this relation within a narrow temperature range, as follows:

$$\Gamma = A + BT, \tag{27}$$

where T is the temperature and A and B are coefficients that vary from tissue to tissue [144]. Higher order terms will be added in Eq. (27) in cases beyond the linear region. Phantom and *ex vivo* experiments have demonstrated that the PA method can monitor sub-degree changes in temperature [144,33,145].

7.2. Monitoring the chemical environment

Optical absorption is not only determined by the molecular formation itself, but also affected by environmental chemical conditions. Ashkenazi *et al.* detected the lifetime of a fluorophore's excited state affected by the environmental oxygen concentration [146]. The basic principle is shown in Fig. 11. Fluorescence lifetime imaging is important for quantitative measure of oxygen concentration, providing valuable information to diagnose cancer. However, traditional fluorescence lifetime detection suffers from low resolution. Thus, the PA method can potentially provide ultrasound resolution for fluorescence lifetime imaging. In addition, other biochemical information could be detected by choosing appropriate sensitive dyes.

7.3. Biological cell detection

Detecting living biological cells *in vivo* or *in vitro* is important for diagnosing and treating several diseases, such as tumor metastasis.

Weight *et al.* [147] detected live melanoma cells *in vitro* flowing through a tube, where the isolated melanoma cells were suspended in a 1.8% saline solution. The PA signal is generated by shining a pulsed laser beam on the melanoma cells and detected using a focused ultrasonic transducer. In addition, the aforementioned PAFC, developed by Zharov *et al.* [148,101], have been demonstrated to detect single cells and bacteria that are bio-conjugated with contrast agents. Fig. 12 demonstrates the mechanism of PAFC, where the pulsed laser beam is focused on the circulation system, with a width of approximately 6 μm. The PA pressure is generated as the target passes through the focused pulsed laser beam and absorbs the EM energy. The advantages of PAFC include high sensitivity, and high specificity by binding interested cells with different contrast agents and using spectroscopic detection.

7.4. Photoacoustic flowmetry

If the absorber moves during the PA process, the PA signal changes. By monitoring the changes in the signal, the speed and orientation of the moving absorber can be detected. Either the PA Doppler (PAD) method and and the M-mode method can be used.

The Doppler effect has been widely used in detecting the speed of moving objects, such as in Doppler ultrasound, Doppler radar detection, and Doppler optical coherent tomography. All these methods are based on the frequency shift in the reflected signal caused by the moving object. In PA Doppler, the detected signal is not the reflected illumination waves; instead, it is the PA signal emitted by the object itself. In other words, PA Doppler is based on the frequency shift in the emitted PA signal from a moving source. Fang *et al.* [149] first reported the PA Doppler effect. They used a continuous illumination source with intensity modulation as given by

$$I(t)=I_0\,[\,1+\cos\,(2\pi f_0 t)]/2\,, \tag{28}$$

where I_0 is the peak intensity and f_0 is the modulation frequency.

The Doppler frequency shift f_{PAD} is

$$f_{PAD}=f_0\frac{V}{c_A}\cos(\theta)\,, \tag{29}$$

where V is the absorber velocity, c_A is the acoustic velocity in the medium, and θ is the relative angle between the detection direction and particle velocity as shown in Fig. 13. They used the lock-in technique to detect the frequency shift. In addition, the lock-in technique also provides the ability to determine the flow direction. PAD has the potential to detect blood flow in microvasculature. However, PAD can not detect speed information from absorbers moving perpendicular to the detection direction, the same as in other Doppler detection methods.

Fang and Wang also developed the M-mode PA flowmetry, which borrows an idea from M-mode ultrasound, measuring the traveling time of an absorber passing through a certain region, such as the focal zone of the transducer [150]. This method is good at detecting flow which is perpendicular to the detection direction.

8. Translational research

Photoacoustics has achieved great success in phantom and animal studies. Currently, more and more research is targeting its clinical applications in humans. Here, we present several works that involve *in vivo* and *ex vivo* human tissues.

8.1. Breast imaging

Breast cancer is the most common cancer in women and the second leading cause of cancer death in women. In the U.S., one in eight women will develop breast cancer in her life. The cure and survival of breast cancer highly depend on how early it is diagnosed and treated. Current routine screening methods are X-ray mammography and ultrasound. However, besides its ionizing hazard, X-ray mammography does not easily detect tumors in dense breasts. In addition, early, small, nonpalpable breast tumors have less acoustic contrast, making them hard to detect by ultrasound. Moreover, ultrasound detection results also depend on the experience and skills of the operator. Thus, innovative breast imaging methods, which are sensitive to the early stage of cancer, are in great need.

As mentioned, the development of tumor is generally accompanied by angiogenesis. In addition, the malignant breast tumor tissue can have higher dielectric conductivity [151], likely due to an increase in water content. Both blood and water are good PA absorbers, as we discussed before. Thus, it has long been shown that breast cancer tissue can be detected by both PAT and TAT. PAT is sensitive to tumor-related vasculature, such as angiogenesis, and to hemorrhagic infiltration; TAT is sensitive to abnormal high dielectric conductivity in cancerous tissue. In addition, spectroscopic PAT can detect cancer's hypoxic characteristic, because the tumor region has lower SO_2 than healthy tissue.

PAT images the breast by using NIR, which can penetrate breast tissue ~ 5 centimeters. Two laser-based PAT breast imaging systems have been developed by researchers at Fairway Medical Technologies Inc. [47] and by Manohar, *et al.* [152], as shown in Fig. 14(a) and (b), respectively. Laser wavelengths used in these systems are 757 nm and 1064 nm. Both systems have been used in clinical study and have demonstrated that PAT can detect breast tumors that are missed by X-ray mammography [47,153]. For instance, Oraevsky *et al*. used the first system and successfully detected a breast cancer that was missed by X-ray mammography [154,47], as shown in Fig. 15.

Breast tumors usually have higher conductivity values than normal breast fat tissue. Thus, RF absorption in breast tumor can be much higher than in normal tissue, especially in breasts with high adipose concentration [157,158]. Currently, two TAT systems have been developed by Kruger *et al.* [155] and by L. V. Wang and G. Ku [159], as shown in Fig. 14(c) and (d), respectively. The latter system can also integrate PAT by switching the illumination source between RF waves and laser [156]. Clinical study results from Kruger *et al.*'s system show TAT signal enhancement in the tumor region [155].

Besides sensitive ultrasonic detectors, other factors need to be considered in developing a PA breast imaging system, including EM radiation delivery and image reconstruction. Due to the light scattering and RF diffraction, the EM radiation fields are generally non-uniform in the breast, which affects the dynamic range and SNR of the PA signal. Using broad illumination as in [47] can generate relatively uniform EM radiation within a section of the breast. Also, mildly compressing the breast can mitigate the problem by reducing the breast thickness, as done in [153]. Moreover, EM shielding is helpful [160] to reduce the direct EM interference between the EM radiation field and the ultrasonic detection system. In addition to EM delivery, the shape of the breast makes it hard or impossible to detect PA pressure waves traveling toward the chest. Thus, the image reconstruction belongs to a limited-view case. To reduce the reconstruction artifacts, new algorithms are being developed. For instance, Patch demonstrated that the unmeasured PA pressure that propagates toward the chest wall can be estimated from the detected data [161]. Iterative methods can also play an important role here. Moreover, image distortion due to the the variance in sound speed is also under studying [162]. We expect that improvements in both techniques and image reconstruction algorithms will foster clinical applications of PA breast imaging.

PAT also aids in breast cancer monitoring and treatment. For instance, sentinel lymph node biopsy is an important method to determine the stage of breast cancer. The traditional method to find the sentinel lymph node is by using a radioactive tracer and methylene blue dye. Both radioactive tracer and methylene blue will be accumulated in the sentinel lymph node. Then, a hand held Geiger counter is used to estimate the rough location of the node. However, this method not only has radiative hazard, but also has a poor spatial resolution. As mentioned, by using laser wavelength at the peak absorption spectrum of methylene blue, PAT can image the sentinel lymph node with high resolution [127], enabling minimally invasive methods to needle-biopsy the node.

8.2. Skin tissue study

Based on ballistic reflected photons, high resolution optical imaging methods have a confined imaging depth up to one transport mean free path, which is ~1.0 mm in the skin. However, skin related diseases, such as burn wounds, melanoma, and port-wine stains, can be more than 1 mm below the skin. In addition, pure optical imaging methods are not sensitive to the absorption, limiting their application in imaging blood microvasculature. PAT overcomes these limits with high resolution.

PAT, especially PAM, is a promising tool to image and detect skin cancer. It has demonstrated the ability to achieve high quality *in vivo* subcutaneous microvasculature images of human skin [97]. By using multiple wavelengths, the oxygen saturation in blood vessels can be detected, which is highly related to tumor hypoxia. In addition, PAT can also aid in port-wine stain treatment by locating blood vessels and melanin in tissue [51,163].

Burn injuries have been studied by several researchers using PA techniques [164,165]. Zhang *et al.* imaged acute thermal burns using the PAM [164], which provides high resolution of burn wounds.

8.3. Brain imaging

Current high resolution brain imaging methods include X-ray computed tomography (CT), MRI, and ultrasound. However, CT uses ionizing radiation and MRI uses a strong magnetic field, and both methods are costly. Ultrasonography can only be used in pediatric brain imaging, and then only before closure of the fontanel. In addition, functional brain images are provided by functional MRI (fMRI), electroencephalography (EEG), magnetoencephalography (MEG), positron emission tomography (PET), single photon emission computed tomography (SPET) and diffuse optical tomography (DOT). Only fMRI, PET and SPET can provide high resolution. But fMRI is expensive and has a low temporal resolution, and PET and SPET use radioactive contrast agents.

Relying on functionally sensitive EM contrast and one-way ultrasonic transportation, PAT has a great potential as a low-cost, real-time and functionally sensitive brain imaging modality. PAT has achieved great success in imaging small animal brains [114,166,167], which have thin skulls. Although a thick skull strongly attenuates and distorts PA pressure waves, PA signals can be detected through a thick skull, based on preliminary experiments on monkey heads and human skull phantoms [89,168].

Because the skull of an infant is much thinner than that of an adult, with an average thickness of 1.3 mm, both light and acoustic waves can penetrate it with less attenuation, enabling transcranial PA imaging. Wang *et al.* [169] first studied *ex vivo* transcranial PAT over a neonatal skull. They used part of a neonatal skull covering fresh canine brain tissue, which has similar optical properties to the human brain. Then, 50 μm diameter tubes filled with canine blood were buried at different depths under the skull, as shown in Fig. 16(a). The skull was illuminated by laser with a wavelength of 850 nm, and the generated PA pressure was detected by a 5-MHz center frequency 1-inch focal length ultrasonic transducer. Their results demonstrated the PA signals generated from up to 21 mm beneath the skull can be detected, as shown in Fig. 16(b,c). They intend to apply this technique to detect brain hypoxia-ischemia cerebral injury. In addition, ultrasound imaging uses the fontanel as a “ultrasonic window” for neonatal brain imaging, and PAT can also take advantage of this window.

Brain imaging of deep tissue or imaging through a thick skull, such as a human skull, is still challenging. The human adult skull has a thickness of about 5 mm. The thick skull not only attenuates illumination intensity and acoustic waves, but also diffracts acoustic waves due to velocity mismatch and mode conversion. Reconstructed images can be blurred strongly without

appropriate correction [89]. Advanced reconstruction algorithms need to be developed by considering the skull bone's acoustic characteristics, which can be measured by other methods, such as CT.

Many tissues have the potential to be PA targets, such as peripheral joint tissues, which were recently imaged by Wang *et al.* [170,57]. In addition, many more translational research projects are being carried out in animal and phantom experiments. We expect more human tissue types to be studied by PA techniques.

9. Summary and discussion

Photoacoustics in biomedicine combines the acoustic detection and EM absorption contrast. The PA signal can be generated using either an EM pulse or an intensity-modulated CW source. Most PA illumination uses the optical region (visible to NIR), and the RF region (including microwaves). The PA signal depends on several variables, such as the absorption ability (the absorption coefficient or dielectric constants), target shape, illumination intensity, and the ultrasound attenuation in medium. Endogenous biological absorbers include blood, melanin, water, etc. Recorded PA signals generally require data processing, including denoising and deconvolution, to recover the original PA pressure.

PAT plays an important role in PA applications. In this article, we categorized the most current PAT into three classes based on their detection methods. The resolution of PAT is scalable, ranging from sub-millimeters to 15 μm, by choosing transducers with different center frequencies and bandwidth. The lateral resolution can be further improved to reach optical resolution (in order of micrometers), by using optical focusing, imaging superficial objects within the optical quasiballistic regime [24]. Both exact and approximate reconstruction algorithms have been developed for PA computed tomography.

PAT can provide not only structural imaging, but also functional imaging by using spectroscopic imaging. In addition, combining PAT with other current biomedical imaging methods forms multi-functional imaging modalities.

PA contrast agents have been extensively studied, including dyes and nanoparticles. Contrast agents can improve the sensitivity and specificity of PA detection. In order to detect deeper into scattering tissue, contrast agents with high absorption in the NIR region are desirable. Moreover, contrast agents enable PA molecular imaging.

Many more physiology characteristic parameters (thermal, chemical, and mechanical parameters), can be monitored by using PA detections. We emphasized on the newly discovered PA Doppler effect in this article. Unlike other Doppler effects caused by frequency changes in the reflected radiation waves by moving objects, PA Doppler effect is caused by the movement of emitters.

Overall, PA techniques for biomedicine are maturing. They have been widely used to study both animal and human tissues. Recently, more and more research focuses on clinical applications. Commercialized PA systems are expected to be available in the near future, and wide clinical PA applications are foreseen.

Acknowledgments

This work has be supported in part by National Institutes of Health grants R01 EB000712, R01 NS46214 (Bioengineering Research Partnerships), R01 EB008085, and U54 CA136398 (Network for Translational Research). L.W. has a financial interest in Microphotoacoustics, Inc. and Endra, Inc., which, however, did not support this work."

References

1. Alexander Graham Bell. On the production of sound by light. American Journal of Science 1880;20:305.
2. Kreuzer LB. Ultralow gas concentration infrared absorption spectroscopy. Journal of Applied Physics 1971;42(7):2934–2943.
3. Rosencwaig, Allan. Photoacoustics and Photoacoustic Spectroscopy. New York: Wiley; 1980. Chemical analysis
4. Gusev, VE.; Karabutov, AA.; Hendzel, Kevin. Laser Optoacoustics. AIP Press; 1993.
5. Maugh Ii, Thomas H. Photoacoustic spectroscopy: New uses for an old technique. Science 1975;188 (4183):38–39. [PubMed: 17760158]
6. Kruger RA. Photoacoustic ultrasound. Medical Physics 1994;21(1):127–131. [PubMed: 8164577]
7. Karabutov AA, Podymova NB, Letokhov VS. Time-resolved laser optoacoustic tomography of inhomogeneous media. Applied Physics B-Lasers and Optics 1996;63(6):545–563.
8. Oraevsky, Alexander A.; Jacques, Steven L.; Esenaliev, Rinat O. Optoacoustic imaging for medical diagnosis. U.S. patent. 5,840,023. 1996.
9. Oraevsky AA, Jacques SL, Tittel FK. Measurement of tissue optical properties by time-resolved detection of laser-induced transient stress. Applied Optics 1997;36(1):402–415. [PubMed: 18250688]
10. Wang LHV, Zhao XM, Sun HT, Ku G. Microwave-induced acoustic imaging of biological tissues. Review of Scientific Instruments 1999;70(9):3744–3748.
11. SPIE. BiOS 2000: International Biomedical Optics Symposium, volume 3916 of Biomedical Optoacoustics; San Jose. SPIE; 2000.
12. SPIE. BiOS 2001: International Biomedical Optics Symposium, volume 4256 of Biomedical Optoacoustics II; San Jose, CA. SPIE; 2001.
13. SPIE. BiOS 2002: International Biomedical Optics Symposium, volume 4618 of Biomedical Optoacoustics III; San Jose, CA. SPIE; 2002.
14. SPIE. BiOS 2003: International Biomedical Optics Symposium, volume 4960 of Biomedical Optoacoustics IV; San Jose, CA. SPIE; 2003.
15. SPIE. BiOS 2004: International Biomedical Optics Symposium, volume 5320 of Photons Plus Ultrasound: Imaging and Sensing; San Jose, CA. SPIE; 2004.
16. SPIE. BiOS 2005: Biomedical Optics, volume 5697 of Photons Plus Ultrasound: Imaging and Sensing 2005: The Sixth Conference on Biomedical Thermoacoustics, Optoacoustics, and Acousto-optics; San Jose, CA. SPIE; 2005.
17. SPIE. BiOS: Biomedical Optics 2006, volume 6086 of Photons Plus Ultrasound: Imaging and Sensing 2006: The Seventh Conference on Biomedical Thermoacoustics, Optoacoustics, and Acousto-optics; San Jose, CA. SPIE; 2006.
18. SPIE. Photonics West: Biomedical Optics (BiOS) 2007, volume 6437 of Photons Plus Ultrasound: Imaging and Sensing 2007: The Eighth Conference on Biomedical Thermoacoustics, Optoacoustics, and Acousto-optics; San Jose, CA. SPIE; 2007.
19. SPIE. Photonics West: Biomedical Optics (BiOS) 2008, volume 6856 of Photons Plus Ultrasound: Imaging and Sensing 2008: The Ninth Conference on Biomedical Thermoacoustics, Optoacoustics, and Acousto-optics; San Jose, CA. SPIE; 2008.
20. Wang LV. Tutorial on photoacoustic microscopy and computed tomography. IEEE Journal of Selected Topics in Quantum Electronics 2008;14(1):171–179.
21. Xu MH, Wang LHV. Photoacoustic imaging in biomedicine. Review of Scientific Instruments 2006;77(4)
22. Patch SK, Scherzer O. Photo- and thermo-acoustic imaging. Inverse Problems 2007;23(6):S1–S10.
23. Oraevsky, A.; Karabutov, A. Optoacoustic tomography. In: Vo-Dinh, T., editor. Biomedical Photonics Handbook. Boca Raton, FL: CRC; 2003.
24. Wang, Lihong V.; Wu, Hsin-i. Biomedical Optics : Principles and Imaging. Hoboken, N.J.: Wiley; 2007.
25. Monici, Monica; El-Gewely, MR. Biotechnology Annual Review. Vol. volume 11. Elsevier; 2005. Cell and tissue autofluorescence research and diagnostic applications; p. 227-256.

26. OMLC. Optical properties spectra. 2001 (http://omlc.ogi.edu/spectra/).
27. Segelstein, DJ. PhD thesis. University of Missouri-Kansas City; 1981. The complex refractive index of water.
28. Jacques, Steven L. Melanosome absorption coefficient. 1998
29. Duck, FA. Physical Properties of Tissue. London: Academic; 1990.
30. Morse, Philip M.; Uno Ingard, K. Theoretical Acoustics. Princeton, New Jersey: Princeton University Press; 1986.
31. Diebold GJ, Sun T, Khan MI. Phtoacoustic monopole radiation in 1-dimention, 2-dimension, and 3-dimension. Physical Review Letters 1991;67(24):3384–3387. [PubMed: 10044720]
32. Li CH, Pramanik M, Ku G, Wang LV. Image distortion in thermoacoustic tomography caused by microwave diffraction. Physical Review E 2008;77(3):031923.
33. Shah J, Park S, Aglyamov S, Larson T, Ma L, Sokolov K, Johnston K, Milner T, Emelianov SY. Photoacoustic imaging and temperature measurement for photothermal cancer therapy. Journal of Biomedical Optics 2008;13(3)
34. Taflov, Allen; Hagness, SC. Computational Electrodynamics: The Finite-Difference Time-Domain Method. 3 edition. Boston, London: Artech House Publishers; 2005.
35. Hagness S. Space-time microwave imaging for breast cancer detection: Theoretical principles and experimental techniques. Medical Physics 2003;30(6):1541–1541.
36. Yee, Kane S. Numerical solution of inital boundary value problems involving maxwell's equations in isotropic media. Antennas and Propagation, IEEE Transactions on 1966;14(3):302–307.
37. Draine BT. The discrete-dipole approximation and its application to interstellar graphite grains. Astrophys. J 1988;333:848–872.
38. Food and Drug Administration. Guidance for industry and FDA staff - information for manufacturers seeking marketing clearance of diagnostic ultrasound systems and transducers. 2008
39. Guittet C, Ossant F, Vaillant L, Berson M. In vivo high-frequency ultrasonic characterization of human dermis. IEEE Transactions on Biomedical Engineering 1999;46(6):740–746. [PubMed: 10356880]
40. Guittet C, Ossant F, Remenieras JP, Pourcelot L, Berson M. High-frequency estimation of the ultrasonic attenuation coefficient slope obtained in human skin: Simulation and in vivo results. Ultrasound in Medicine and Biology 1999;25(3):421–429. [PubMed: 10374985]
41. Sivaramakrishnan M, Maslov K, Zhang HF, Stoica G, Wang LV. Limitations of quantitative photoacoustic measurements of blood oxygenation in small vessels. Physics in Medicine and Biology 2007;52(5):1349–1361. [PubMed: 17301459]
42. Laser Institute of America. American national standard for safe use of lasers 2000;Z136:1–2000.
43. Institute of Electrical and Electronics Engineers (IEEE). IEEE standard for safety levels with respect to human exposure to radio frequency electromagnetic fields 3 kHz to 300 GHz. 1999
44. Department of Health Services and Human. Food and drug administration modernization act of 1997; modifications to the list of recognized standards, recognition list number: 011. 2004
45. Donoho DL, Johnstone IM. Adapting to unknown smoothness via wavelet shrinkage. Journal of the American Statistical Association 1995;90(432):1200–1224.
46. Taswell, Carl. The what, how, and why of wavelet shrinkage denoising. Technical Report CT-1998-09, Computational Toolsmiths. 1998.
47. Ermilov, Sergey A.; Khamapirad, Tuenchit; Conjusteau, Andre; Leonard, Morton H.; Lacewell, Ron; Mehta, Ketan; Miller, Tom; Oraevsky, Alexander A. Laser optoacoustic imaging system for detection of breast cancer. Journal of Biomedical Optics 2009;14(2):024007–024014. [PubMed: 19405737]
48. Vetterli M, Herley C. Wavelets and filter banks - theory and design. IEEE Transactions on Signal Processing 1992;40(9):2207–2232.
49. Burrus, CS.; Gopinath, RA.; Guo, H. Introduction to Wavelets and Wavelet Transforms: A Primer. Upper Saddle River, NJ: Prentice Hall; 1998.
50. Kaiser, Gerald. A Friendly Guide to Wavelets. Boston: Birkh?user; 1994.
51. Viator JA, Choi B, Ambrose M, Spanier J, Nelson JS. In vivo port-wine stain depth determination with a photoacoustic probe. Applied Optics 2003;42(16):3215–3224. [PubMed: 12790472]

52. Holan SH, Viator JA. Automated wavelet denoising of photoacoustic signals for circulating melanoma cell detection and burn image reconstruction. Physics in Medicine and Biology 2008;53(12):N227–N236. [PubMed: 18495977]
53. Zeng LM, Xing D, Gu HM, Yang DW, Yang SH, Xiang LZ. High antinoise photoacoustic tomography based on a modified filtered backprojection algorithm with combination wavelet. Medical Physics 2007;34(2):556–563. [PubMed: 17388173]
54. Kruger RA, Kiser WL, Reinecke DR, Kruger GA. Thermoacoustic computed tomography using a conventional linear transducer array. Medical Physics 2003;30(5):856–860. [PubMed: 12772993]
55. Gamelin J, Aguirre A, Maurudis A, Huang F, Castillo D, Wang LV, Zhu Q. Curved array photoacoustic tomographic system for small animal imaging. Journal of Biomedical Optics 2008;13:024007. [PubMed: 18465970]
56. Wang XD, Pang YJ, Ku G, Xie XY, Stoica G, Wang LHV. Noninvasive laser-induced photoacoustic tomography for structural and functional in vivo imaging of the brain. Nature Biotechnology 2003;21(7):803–806.
57. Wang XD, Chamberland DL, Jamadar DA. Noninvasive photoacoustic tomography of human peripheral joints toward diagnosis of inflammatory arthritis. Optics Letters 2007;32(20):3002–3004. [PubMed: 17938680]
58. Li, Changhui; Ku, Geng; Wang, Lihong. V Negative lens concept for photoacoustic tomography. Physical Review E 2008;78(2):021901.
59. Zhang E, Laufer J, Beard P. Backward-mode multiwavelength photoacoustic scanner using a planar fabry-perot polymer film ultrasound sensor for high-resolution three-dimensional imaging of biological tissues. Applied Optics 2008;47(4):561–577. [PubMed: 18239717]
60. Beard, Paul C.; Perennes, Frederic; Mills, Tim N. Transduction mechanisms of the fabry-perot polymer film sensing concept for wideband ultrasound detection. IEEE Trans. Ultrason. Ferroelectr. Freq. Control 1999;46 1575C1582.
61. Haltmeier M, Scherzer O, Burgholzer P, Paltauf G. Thermoacoustic computed tomography with large planar receivers. Inverse Problems 2004;20(5):1663–1673.
62. Paltauf G, Nuster R, Haltmeier M, Burgholzer P. Photoacoustic tomography using a mach-zehnder interferometer as an acoustic line detector. Applied Optics 2007;46(16):3352–3358. [PubMed: 17514293]
63. Yang DW, Xing D, Yang SH, Xiang LZ. Fast full-view photoacoustic imaging by combined scanning with a linear transducer array. Optics Express 2007;15(23):15566–15575. [PubMed: 19550843]
64. Witte RS, Kim K, Agarwal A, Fan W, Kopelman R, Kotov N, Kipke D, O'Donnell M. Enhanced photoacoustic neuroimaging with gold nanorods and pebbles. Proceedings of the SPIE - The International Society for Optical Engineering 2008;6856:685614.
65. Niederhauser JJ, Jaeger M, Lemor R, Weber P, Frenz M. Combined ultrasound and optoacoustic system for real-time high-contrast vascular imaging in vivo. IEEE Transactions on Medical Imaging 2005;24(4):436–440. [PubMed: 15822801]
66. Zemp RJ, Bitton R, Li ML, Shung KK, Stoica G, Wang LV. Photoacoustic imaging of the microvasculature with a high-frequency ultrasound array transducer. Journal of Biomedical Optics 2007;12:010501. [PubMed: 17343475]
67. Zemp RJ, Song LA, Bitton R, Shung KK, Wang LHV. Realtime photoacoustic microscopy in vivo with a 30-mhz ultrasound array transducer. Optics Express 2008;16(11):7915–7928. [PubMed: 18545502]
68. Gamelin, John; Maurudis, Anastasios; Aguirre, Andres; Huang, Fei; Guo, Puyun; Wang, Lihong V.; Zhu, Quing. A real-time photoacoustic tomography system for small animals. Opt. Express 2009;17(13):10489–10498. [PubMed: 19550444]
69. Kuchment, Peter; Kunyansky, Leonid. A survey in mathematics for industry: mathematics of thermoacoustic tomography. Euro. Jnl of Applied Mathematics 2008;19:191–224.
70. Finch, David; Patch, Sarah K.; RAKESH. Determining a function from its mean values over a family of spheres. SIAM Journal on Mathematical Analysis 2004;35(5):1213–1240.
71. Kunyansky, Leonid A. Explicit inversion formulae for the spherical mean radon transform. Inverse Problems 2007;23(1):373–383.

72. Kostli KP, Frenz M, Bebie H, Weber HP. Temporal backward projection of optoacoustic pressure transients using fourier transform methods. Physics in Medicine and Biology 2001;46(7):1863–1872. [PubMed: 11474930]
73. Norton, Stephen J.; Melvin, Linzer. Ultrasonic reflectivity imaging in three dimensions: Exact inverse scattering solutions for plane, cylindrical, and spherical apertures. Biomedical Engineering, IEEE Transactions on 1981;28(2):202–220.
74. Xu, Minghua; Wang, LV. Time-domain reconstruction for thermoacoustic tomography in a spherical geometry. Medical Imaging, IEEE Transactions on 2002;21(7):814–822.
75. Xu, Yuan; Feng, Dazi; WANG, Lihong V. Exact frequency-domain reconstruction for thermoacoustic tomography. i. planar geometry. IEEE transactions on medical imaging 2002;21(7):823–828. [PubMed: 12374319]
76. Xu, Yuan; Xu, Minghua; Wang, LV. Exact frequency-domain reconstruction for thermoacoustic tomography. ii. cylindrical geometry. Medical Imaging, IEEE Transactions on 2002;21(7):829–833.
77. Xu MH, Wang LHV. Universal back-projection algorithm for photoacoustic computed tomography. Physical Review E 2005;71:016706.
78. Xu MH, Wang LV. Universal back-projection algorithm for photoacoustic computed tomography (vol 71, art no 016706, 2005). Physical Review E 2007;75:059903.
79. Kunyansky, Leonid A. A series solution and a fast algorithm for the inversion of the spherical mean radon transform. Inverse Problems 2007;23(6):S11–S20.
80. Burgholzer P, Matt GJ, Haltmeier M, Paltauf G. Exact and approximative imaging methods for photoacoustic tomography using an arbitrary detection surface. Physical Review E 2007;75:046706.
81. Xu Y, Wang LHV. Time reversal and its application to tomography with diffracting sources. Physical Review Letters 2004;92(3):033902. [PubMed: 14753876]
82. Xu MH, Wang LV. Analytic explanation of spatial resolution related to bandwidth and detector aperture size in thermoacoustic or photoacoustic reconstruction. Physical Review E 2003;67(5): 056605.
83. Burgholzer P, Hofer C, Paltauf G, Haltmeier M, Scherzer O. Thermoacoustic tomography with integrating area and line detectors. IEEE Transactions on Ultrasonics Ferroelectrics and Frequency Control 2005;52(9):1577–1583.
84. Burgholzer P, Bauer-Marschallinger J, Grun H, Haltmeier M, Paltauf G. Temporal back-projection algorithms for photoacoustic tomography with integrating line detectors. Inverse Problems 2007;23 (6):65–80.
85. Kruger RA, Reynolds HE, Kiser W, Reinecke DR, Kruger GA. Thermoacoustic computed tomography for breast imaging. Radiology 1999;210(2):587–587.
86. Kostli KP, Beard PC. Two-dimensional photoacoustic imaging by use of fourier-transform image reconstruction and a detector with an anisotropic response. Applied Optics 2003;42(10):1899–1908. [PubMed: 12683772]
87. Jaeger M, Schupbach S, Gertsch A, Kitz M, Frenz M. Fourier reconstruction in optoacoustic imaging using truncated regularized inverse k-space interpolation. Inverse Problems 2007;23(6):S51–S63.
88. Paltauf G, Viator JA, Prahl SA, Jacques SL. Iterative reconstruction algorithm for optoacoustic imaging. Journal of the Acoustical Society of America 2002;112(4):1536–1544. [PubMed: 12398460]
89. Yang X, Wang LV. Monkey brain cortex imaging by photoacoustic tomography. Journal of Biomedical Optics 2008;13(4):044009–0440095. [PubMed: 19021337]
90. Zhang, J.; Wang, K.; Yang, Y.; Anastasio, MA. Simultaneous reconstruction of speed-of-sound and optical absorption properties in photoacoustic tomography via a time-domain iterative algorithm. Proceedings of the SPIE - The International Society for Optical Engineering; San Jose, CA, USA. 2008. p. 68561
91. Lustig M, Donoho D, Pauly JM. Sparse mri: The application of compressed sensing for rapid mr imaging. Magnetic Resonance in Medicine 2007;58(6):1182–1195. [PubMed: 17969013]
92. Provost, Jean; Lesage, Frederic. The application of compressed sensing for photo-acoustic tomography. IEEE Trans Med Imaging 2009;28(4):585–594. [PubMed: 19272991]

93. Yuan Z, Zhang QZ, Jiang HB. Simultaneous reconstruction of acoustic and optical properties of heterogeneous media by quantitative photoacoustic tomography. Optics Express 2006;14(15):6749–6754. [PubMed: 19516856]
94. Laufer J, Delpy D, Elwell C, Beard P. Quantitative spatially resolved measurement of tissue chromophore concentrations using photoacoustic spectroscopy: application to the measurement of blood oxygenation and haemoglobin concentration. Physics in Medicine and Biology 2007;52(1): 141–168. [PubMed: 17183133]
95. Maslov K, Stoica G, Wang LVH. In vivo dark-field reflection-mode photoacoustic microscopy. Optics Letters 2005;30(6):625–627. [PubMed: 15791997]
96. Song KH, Wang LV. Deep reflection-mode photoacoustic imaging of biological tissue. Journal of Biomedical Optics 2007;12:060503. [PubMed: 18163798]
97. Zhang HF, Maslov K, Stoica G, Wang LHV. Functional photoacoustic microscopy for high-resolution and noninvasive in vivo imaging. Nature Biotechnology 2006;24(7):848–851.
98. Li ML, Zhang HF, Maslov K, Stoica G, Wang LHV. Improved in vivo photoacoustic microscopy based on a virtual-detector concept. Optics Letters 2006;31(4):474–476. [PubMed: 16496891]
99. Maslov K, Zhang HF, Hu S, Wang LV. Optical-resolution photoacoustic microscopy for in vivo imaging of single capillaries. Optics Letters 2008;33(9):929–931. [PubMed: 18451942]
100. Kong F, Chen YC, Lloyd HO, Silverman RH, Kim HH, Cannata JM, Shung KK. High-resolution photoacoustic imaging with focused laser and ultrasonic beams. Applied Physics Letters 2009;94 (3):3.
101. Zharov VP, Galanzha EI, Shashkov EV, Kim JW, Khlebtsov NG, Tuchin VV. Photoacoustic flow cytometry: principle and application for real-time detection of circulating single nanoparticles, pathogens, and contrast dyes in vivo. Journal of Biomedical Optics 2007;12(5):051503. [PubMed: 17994867]
102. Niederhauser JJ, Jaeger M, Frenz M. Real-time three-dimensional optoacoustic imaging using an acoustic lens system. Applied Physics Letters 2004;85(5):846–848.
103. Chen ZX, Tang ZL, Wan W. Photoacoustic tomography imaging based on a 4f acoustic lens imaging system. Optics Express 2007;15(8):4966–4976. [PubMed: 19532746]
104. Kolkman RGM, Hondebrink E, Steenbergen W, van Leeuwen TG, de Mul FFM. Photoacoustic imaging of blood vessels with a double-ring sensor featuring a narrow angular aperture. Journal of Biomedical Optics 2004;9(6):1327–1335. [PubMed: 15568955]
105. Telenkov SA, Mandelis A. Fourier-domain biophotoacoustic subsurface depth selective amplitude and phase imaging of turbid phantoms and biological tissue. Journal of Biomedical Optics 2006;11 (4):044006. [PubMed: 16965163]
106. Maslov K, Wang LV. Photoacoustic imaging of biological tissue with intensity-modulated continuous-wave laser. Journal of Biomedical Optics 2008;13(2)
107. Yang S, Xing D, Zhou Q, Xiang L, Lao Y. Functional imaging of cerebrovascular activities in small animals using high-resolution photoacoustic tomography. Medical Physics 2007;34(8):3294–3301. [PubMed: 17879793]
108. Zemp RJ, Song L, Bitton R, Shung KK, Wang LV. Realtime photoacoustic microscopy of murine cardiovascular dynamics. Optics Express 2008;16(22):18551–18556. [PubMed: 18958134]
109. Zhang HF, Maslov K, Sivaramakrishnan M, Stoica G, Wang LHV. Imaging of hemoglobin oxygen saturation variations in single vessels in vivo using photoacoustic microscopy. Applied Physics Letters 2007;90:053901.
110. Kiser WL Jr, Kruger RA, Reinecke DR, Kruger GA, Miller KD. Thermoacoustic in vivo determination of blood oxygenation. Proceedings of the SPIE - The International Society for Optical Engineering 2004;5320(1):1–7.
111. Stantz KM, Liu B, Cao M, Reinecke D, Miller K, Kruger R. Photoacoustic spectroscopic imaging of intra-tumor heterogeneity and molecular identification - art. no. 608605. Photons Plus Ultrasound: Imaging and Sensing 2006 2006;volume 6086:8605–8605.
112. Maslov K, Zhang HF, Wang LV. Effects of wavelength-dependent fluence attenuation on the noninvasive photoacoustic imaging of hemoglobin oxygen saturation in subcutaneous vasculature in vivo. Inverse Problems 2007;23(6):S113–S122.

113. Li ML, Oh JT, Xie XY, Ku G, Wang W, Li C, Lungu G, Stoica G, Wang LV. Simultaneous molecular and hypoxia imaging of brain tumors in vivo using spectroscopic photoacoustic tomography. Proceedings of the IEEE 2008;96(3):481–489.
114. Wang XD, Xie XY, Ku GN, Wang LHV. Noninvasive imaging of hemoglobin concentration and oxygenation in the rat brain using high-resolution photoacoustic tomography. Journal of Biomedical Optics 2006;11:024015. [PubMed: 16674205]
115. Zhang, Hao F.; Maslov, Konstantin; Li, Meng-Lin; Stoica, George; Wang, Lihong V. In vivo volumetric imaging of subcutaneous microvasculature by photoacoustic microscopy. Opt. Express 2006;14(20):9317–9323. [PubMed: 19529315]
116. Yuan Z, Jiang HB. Quantitative photoacoustic tomography: Recovery of optical absorption coefficient maps of heterogeneous media. Applied Physics Letters 2006;88(23):231101–231103.
117. Cox BT, Arridge SR, Beard PC. Estimating chromophore distributions from multiwavelength photoacoustic images. J. Opt. Soc. Am. A 2009;26(2):443–455.
118. Petrov YY, Petrova IY, Patrikeev IA, Esenaliev RO, Prough DS. Multiwavelength optoacoustic system for noninvasive monitoring of cerebral venous oxygenation: a pilot clinical test in the internal jugular vein. Optics Letters 2006;31(12):1827–1829. [PubMed: 16729084]
119. Laufer J, Elwell C, Delpy D, Beard P. In vitro measurements of absolute blood oxygen saturation using pulsed near-infrared photoacoustic spectroscopy: accuracy and resolution. Physics in Medicine and Biology 2005;50(18):4409–4428. [PubMed: 16148401]
120. Sethuraman S, Amirian JH, Litovsky SH, Smalling RW, Emelianov SY. Spectroscopic intravascular photoacoustic imaging to differentiate atherosclerotic plaques. Optics Express 2008;16(5):3362–3367. [PubMed: 18542427]
121. Copland JA, Eghtedari M, Popov VL, Kotov N, Mamedova N, Motamedi M, Oraevsky AA. Bioconjugated gold nanoparticles as a molecular based contrast agent: Implications for imaging of deep tumors using optoacoustic tomography. Molecular Imaging and Biology 2004;6(5):341–349. [PubMed: 15380744]
122. Oraevsky, Alexander A.; Henrichs, Paul M. High contrast optoacoustic imaging using nanoparticles. U.S. patent. 10/764,213. 2004.
123. Ku G, Wang LHV. Deeply penetrating photoacoustic tomography in biological tissues enhanced with an optical contrast agent. Optics Letters 2005;30(5):507–509. [PubMed: 15789718]
124. Wang YW, Xie XY, Wang XD, Ku G, Gill KL, O'Neal DP, Stoica G, Wang LV. Photoacoustic tomography of a nanoshell contrast agent in the in vivo rat brain. Nano Letters 2004;4(9):1689–1692.
125. Wang XD, Ku G, Wegiel MA, Bornhop DJ, Stoica G, Wang LHV. Noninvasive photoacoustic angiography of animal brains in vivo with near-infrared light and an optical contrast agent. Optics Letters 2004;29(7):730–732. [PubMed: 15072373]
126. Yang XM, Skrabalak SE, Li ZY, Xia YN, Wang LHV. Photoacoustic tomography of a rat cerebral cortex in vivo with au nanocages as an optical contrast agent. Nano Letters 2007;7(12):3798–3802. [PubMed: 18020475]
127. Hyun Song, Kwang; Stein, Erich W.; Margenthaler, Julie A.; Wang, Lihong V. Noninvasive photoacoustic identification of sentinel lymph nodes containing methylene blue in vivo in a rat model. Journal of Biomedical Optics 2008;13(5):054033–054036. [PubMed: 19021413]
128. De La Zerda A, Zavaleta C, Keren S, Vaithilingam S, Bodapati S, Liu Z, Levi J, Smith BR, Ma TJ, Oralkan O, Cheng Z, Chen XY, Dai HJ, Khuri-Yakub BT, Gambhir SS. Carbon nanotubes as photoacoustic molecular imaging agents in living mice. Nature Nanotechnology 2008;3(9):557–562.
129. Agarwal A, Huang SW, O'Donnell M, Day KC, Day M, Kotov N, Ashkenazi S. Targeted gold nanorod contrast agent for prostate cancer detection by photoacoustic imaging. Journal of Applied Physics 2007;102(6)
130. Kim K, Huang SW, Ashkenazi S, O'Donnell M, Agarwal A, Kotov NA, Denny MF, Kaplan MJ. Photoacoustic imaging of early inflammatory response using gold nanorods. Applied Physics Letters 2007;90:223901.

131. Chamberland DL, Agarwal A, Kotov N, Fowlkes JB, Carson PL, Wang X. Photoacoustic tomography of joints aided by an etanercept-conjugated gold nanoparticle contrast agent - an ex vivo preliminary rat study. Nanotechnology 2008;19(9):095101.

132. Eghtedari M, Oraevsky A, Copland JA, Kotov NA, Conjusteau A, Motamedi M. High sensitivity of in vivo detection of gold nanorods using a laser optoacoustic imaging system. Nano Letters 2007;7(7):1914–1918. [PubMed: 17570730]

133. Nie LM, Xing D, Yang DW, Zeng LM. Microwave-induced thermoacoustic imaging enhanced with a microwave contrast agent. Complex Medical Engineering, 2007. CME 2007. IEEE/ICME International Conference on 2007:989–993.

134. Pramanik, M.; Ku, G.; Li, CH.; Swierczewska, M.; Green, D.; Sitharaman, B.; Wang, LV. SPIE BIOS: Biomedical Optics. Vol. volume 7177. San Jose, CA: SPIE; 2009. Novel breast cancer detection system combining both thermoacoustic (ta) and photoacoustic (pa) tomography using carbon nanotubes (cnts) as a dual contrast agent. (to be published)

135. Li L, Zemp RJ, Lungu G, Stoica G, Wang LHV. Photoacoustic imaging of lacz gene expression in vivo. Journal of Biomedical Optics 2007;12(2):020504. [PubMed: 17477703]

136. Sethuraman S, Aglyamov SR, Amirian JH, Smalling RW, Emelianov SY. Intravascular photoacoustic imaging using an ivus imaging catheter. IEEE Transactions on Ultrasonics Ferroelectrics and Frequency Control 2007;54(5):978–986.

137. Yang, Joon-Mo; Maslov, Konstantin; Yang, Hao-Chung; Zhou, Qifa; Kirk Shung, K.; Wang, Lihong V. Photoacoustic endoscopy. Opt. Lett 2009;34(10):1591–1593. [PubMed: 19448831]

138. Razansky D, Ntziachristos V. Hybrid photoacoustic fluorescence molecular tomography using finite-element-based inversion. Medical Physics 2007;34(11):4293–4301. [PubMed: 18072494]

139. Welch, AJ.; Van Gemert, MJC., editors. Optical-Thermal Response of Laser-Irradiated Tissue. 1 edition. New York: Plenum Publishing Corporation; 1995.

140. Varghese T, Zagzebski JA, Chen Q, Techavipoo U, Frank G, Johnson C, Wright A, Lee FT. Ultrasound monitoring of temperature change during radiofrequency ablation: Preliminary in-vivo results. Ultrasound in Medicine and Biology 2002;28(3):321–329. [PubMed: 11978412]

141. MaassMoreno R, Damianou CA. Noninvasive temperature estimation in tissue via ultrasound echo-shifts .1. analytical model. Journal of the Acoustical Society of America 1996;100(4):2514–2521. [PubMed: 8865654]

142. Young IR, Hand JW, Oatridge A, Prior MV. Modeling and observation of temperature-changes in-vivo using mri. Magnetic Resonance in Medicine 1994;32(3):358–369. [PubMed: 7984068]

143. Bertsch F, Mattner J, Stehling MK, Muller-Lisse U, Peller M, Loeffler R, Weber J, Messmer K, Wilmanns W, Issels R, Reiser M. Non-invasive temperature mapping using mri: Comparison of two methods based on chemical shift and t-1-relaxation. Magnetic Resonance Imaging 1998;16(4): 393–403. [PubMed: 9665550]

144. Larina IV, Larin KV, Esenaliev RO. Real-time optoacoustic monitoring of temperature in tissues. Journal of Physics D-Applied Physics 2005;38(15):2633–2639.

145. Kandulla J, Elsner H, Birngruber R, Brinkmann R. Noninvasive optoacoustic online retinal temperature determination during continuous-wave laser irradiation. Journal of Biomedical Optics 2006;11:041111. [PubMed: 16965139]

146. Ashkenazi S, Huang SW, Horvath T, Koo YEL, Kopelman R. Photoacoustic probing of fluorophore excited state lifetime with application to oxygen sensing. Journal of Biomedical Optics 2008;13(3): 034023. [PubMed: 18601568]

147. Weight RM, Viator JA, Dale PS, Caldwell CW, Lisle AE. Photoacoustic detection of metastatic melanoma cells in the human circulatory system. Optics Letters 2006;31(20):2998–3000. [PubMed: 17001379]

148. Zharov VP, Galanzha EI, Shashkov EV, Khlebtsov NG, Tuchin VV. In vivo photoacoustic flow cytometry for monitoring of circulating single cancer cells and contrast agents. Optics Letters 2006;31(24):3623–3625. [PubMed: 17130924]

149. Fang H, Maslov K, Wang LV. Photoacoustic doppler effect from flowing small light-absorbing particles. Physical Review Letters 2007;99(18):184501. [PubMed: 17995411]

150. Fang, Hui; Wang, Lihong V. M-mode photoacoustic particle flow imaging. Opt. Lett 2009;34(5): 671–673. [PubMed: 19252588]

151. Fenn, AJ. Breast Cancer Treatment by Focused Microwave Thermotherapy. 1st edition. Jones and Bartlett Pub; 2006.

152. Manohar S, Kharine A, van Hespen JCG, Steenbergen W, van Leeuwen TG. The twente photoacoustic mammoscope: system overview and performance. Physics in Medicine and Biology 2005;50(11):2543–2557. [PubMed: 15901953]

153. Manohar S, Vaartjes SE, van Hespen JCG, Klaase JM, van den Engh FM, Steenbergen W, van Leeuwen TG. Initial results of in vivo non-invasive cancer imaging in the human breast using near-infrared photoacoustics. Optics Express 2007;15(19):12277–12285. [PubMed: 19547596]

154. Oraevsky AA, Ermilov SA, Conjusteau A, Miller T, Gharieb RR, Lacewell R, Mehta K, Radulescu EG, Herzog D, Thompson S, Stein A, McCorvey M, Otto P, Khamapirad T. Initial clinical evaluation of laser optoacoustic imaging system for diagnostic imaging of breast cancer. Breast Cancer Research and Treatment 2007;106:S47-S47–S47-S47.

155. Kruger RA, Miller KD, Reynolds HE, Kiser WL, Reinecke DR, Kruger GA. Breast cancer in vivo: Contrast enhancement with thermoacoustic ct at 434 mhz - feasibility study. Radiology 2000;216 (1):279–283. [PubMed: 10887262]

156. Pramanik M, Ku G, Li CH, Wang LV. Design and evaluation of a novel breast cancer detection system combining both thermoacoustic (ta) and photoacoustic (pa) tomography. Medical Physics 2008;35(6):2218–2223. [PubMed: 18649451]

157. Lazebnik M, McCartney L, Popovic D, Watkins CB, Lindstrom MJ, Harter J, Sewall S, Magliocco A, Booske JH, Okoniewski M, Hagness SC. A large-scale study of the ultrawideband microwave dielectric properties of normal breast tissue obtained from reduction surgeries. Physics in Medicine and Biology 2007;52(10):2637–2656. [PubMed: 17473342]

158. Lazebnik M, Popovic D, McCartney L, Watkins CB, Lindstrom MJ, Harter J, Sewall S, Ogilvie T, Magliocco A, Breslin TM, Temple W, Mew D, Booske JH, Okoniewski M, Hagness SC. A large-scale study of the ultrawideband microwave dielectric properties of normal, benign and malignant breast tissues obtained from cancer surgeries. Physics in Medicine and Biology 2007;52(20):6093–6115. [PubMed: 17921574]

159. Wang LHV, Ku G. Photoacoustic and thermoacoustic tomography for breast imaging. 2007 (U.S. patent 11/625,099).

160. Mitchell, M.; Becker, G.; Dey, P.; Generotzky, J.; Patch, SK. Shielding for thermoacoustic tomography with rf excitation. Proceedings of the SPIE - The International Society for Optical Engineering; San Jose, CA. SPIE; 2008. 68560X–1–4

161. Patch SK. Thermoacoustic tomography - consistency conditions and the partial scan problem. Physics in Medicine and Biology 2004;49(11):2305–2315. [PubMed: 15248579]

162. Modgil D, Anastasio MA, Wang Kun, La Riviere PJ. Image reconstruction in photoacoustic tomography with variable speed of sound using a higher order geometrical acoustics approximation. Proceedings of the SPIE - The International Society for Optical Engineering 2009;volume 7177 71771A.

163. Kolkman RGM, Mulder MJ, Glade CP, Steenbergen W, van Leeuwen TG. Photoacoustic imaging of port-wine stains. Lasers in Surgery and Medicine 2008;40(3):178–182. [PubMed: 18366079]

164. Zhang HF, Maslov K, Stoica G, Wang LHV. Imaging acute thermal burns by photoacoustic microscopy. Journal of Biomedical Optics 2006;11(5):054033. [PubMed: 17092182]

165. Talbert RJ, Holan SH, Viator JA. Photoacoustic discrimination of viable and thermally coagulated blood using a two-wavelength method for burn injury monitoring. Physics in Medicine and Biology 2007;52(7):1815–1829. [PubMed: 17374913]

166. Maslov, K.; Stein, EW.; Wang, LV. Photoacoustic microscopy of cerebral blood-oxygenation dynamics in mice. Proceedings of the SPIE - The International Society for Optical Engineering; San Jose, CA. SPIE; 2009. p. 1171770C

167. Laufer J, Zhang E, Raivich G, Beard P. Three-dimensional noninvasive imaging of the vasculature in the mouse brain using a high resolution photoacoustic scanner. Applied Optics 2009;48 (10):D299–D306. [PubMed: 19340121]

168. Jin X, Li CH, Wang LV. Effects of acoustic heterogeneities on transcranial brain imaging with microwave-induced thermoacoustic tomography. Medical Physics 2008;35(7):3205–3214. [PubMed: 18697545]

169. Wang XD, Chamberland DL, Xi GH. Noninvasive reflection mode photoacoustic imaging through infant skull toward imaging of neonatal brains. Journal of Neuroscience Methods 2008;168(2):412–421. [PubMed: 18155298]

170. Wang XD, Chamberland DL, Carson PL, Fowlkes JB, Bude RO, Jamadar DA, Roessler BJ. Imaging of joints with laser-based photoacoustic tomography: An animal study. Medical Physics 2006;33 (8):2691–2697. [PubMed: 16964846]

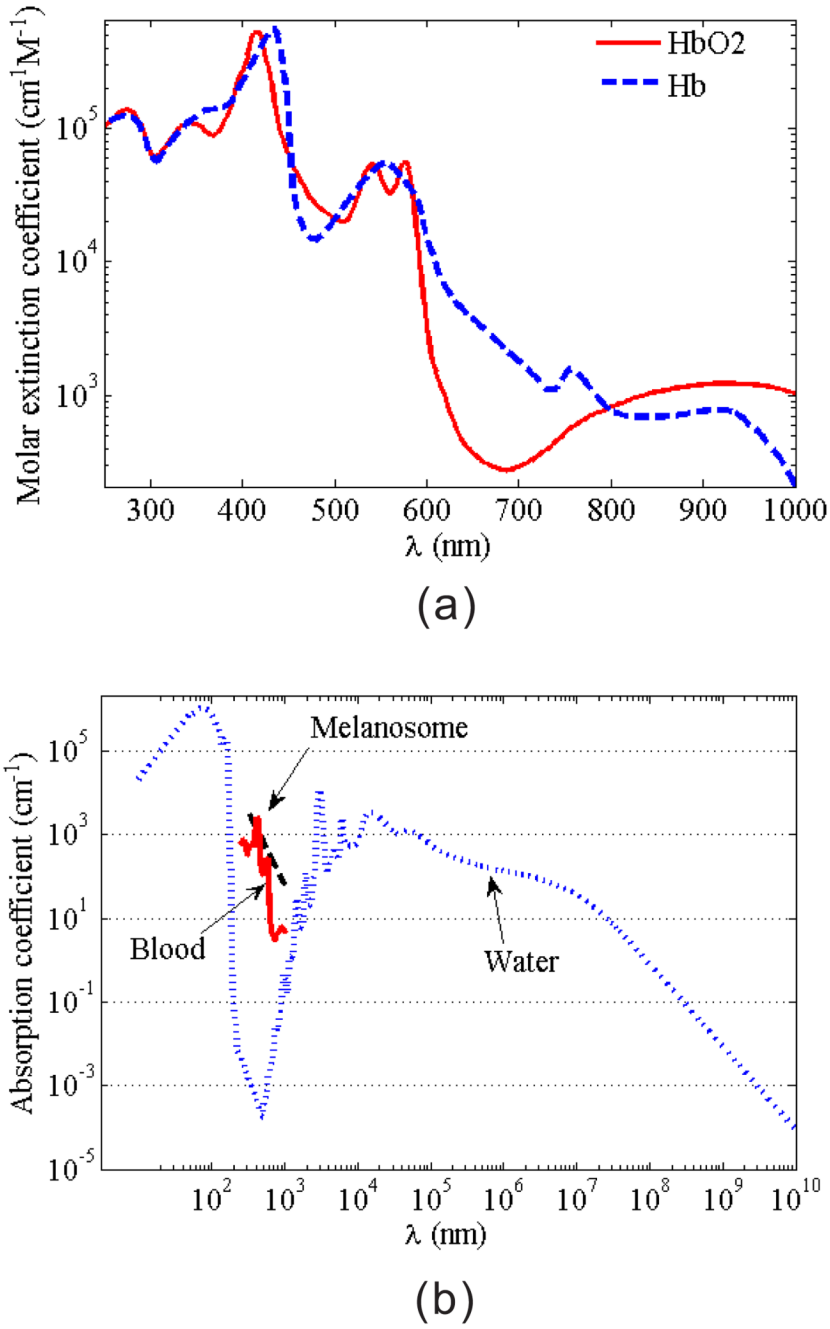

Figure 1.
(Color online) (a) Molar extinction coefficients of oxygenated and de-oxygenated hemoglobin; (b) absorption coefficients of melanosomes, blood (at SO_2=80% and total hemoglobin concentration of 2.33×10^{-3} mol/L), and water.

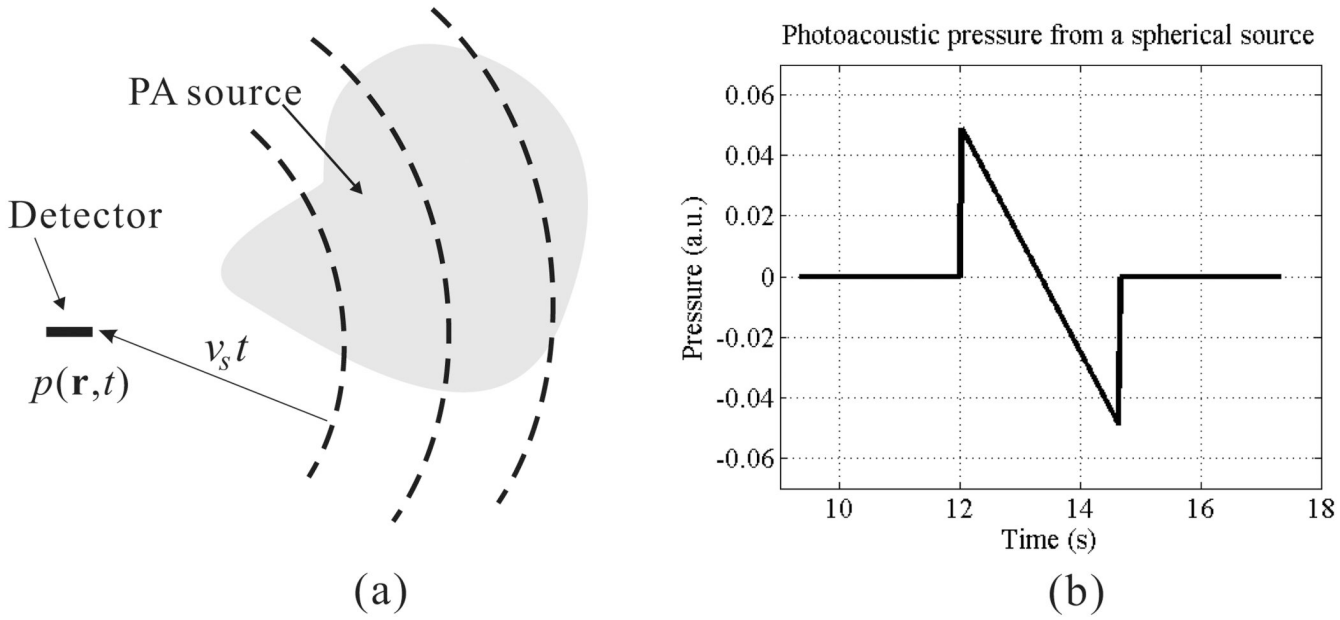

Figure 2.
(a) The PA waves detected by a point detector at a certain time *t* come from sources over a spherical shell centered at the detector position and a radius of $v_s t$. (b) An example of the pressure generated by an uniform spherical PA source.

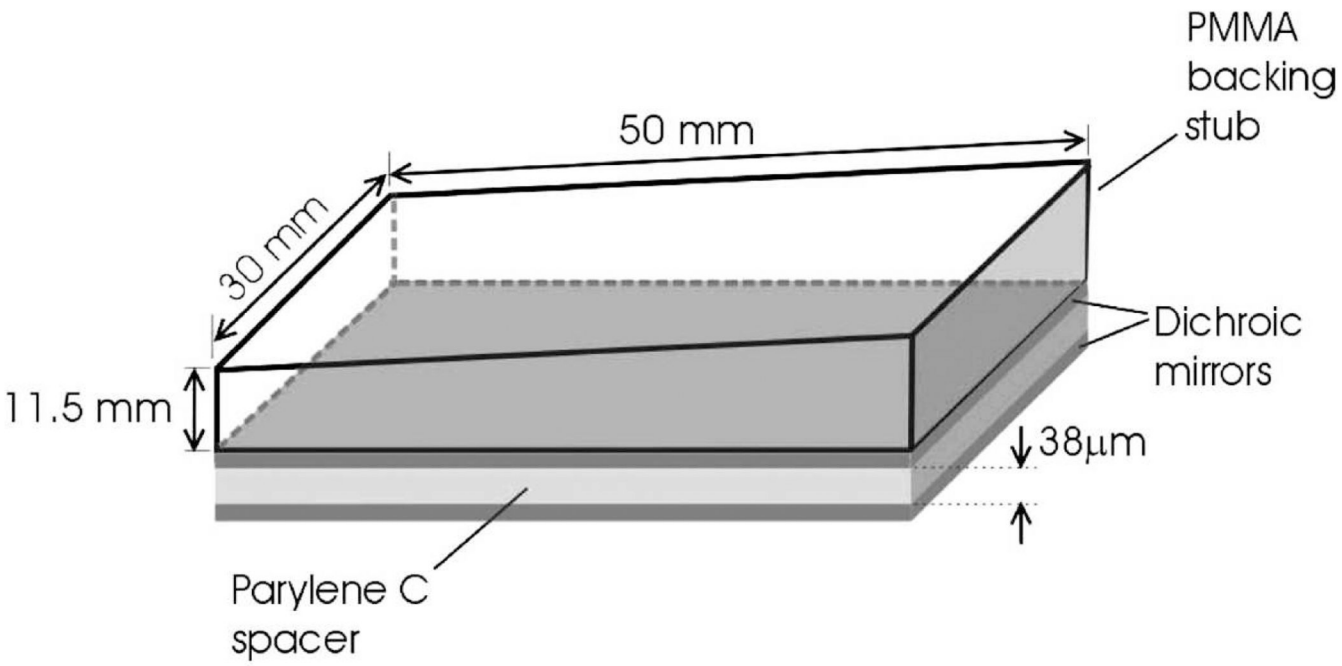

Figure 3.
Schematic of FP sensor head. The sensing structure comprises a 38 μm polymer (Parylene C) film spacer sandwiched between two dichroic mirrors, forming an FPI. The latter overlays a PMMA backing stub that is wedged to eliminate parasitic interference between light reflected from its upper surface and the FPI. Reprinted with permission from Ref. [59]

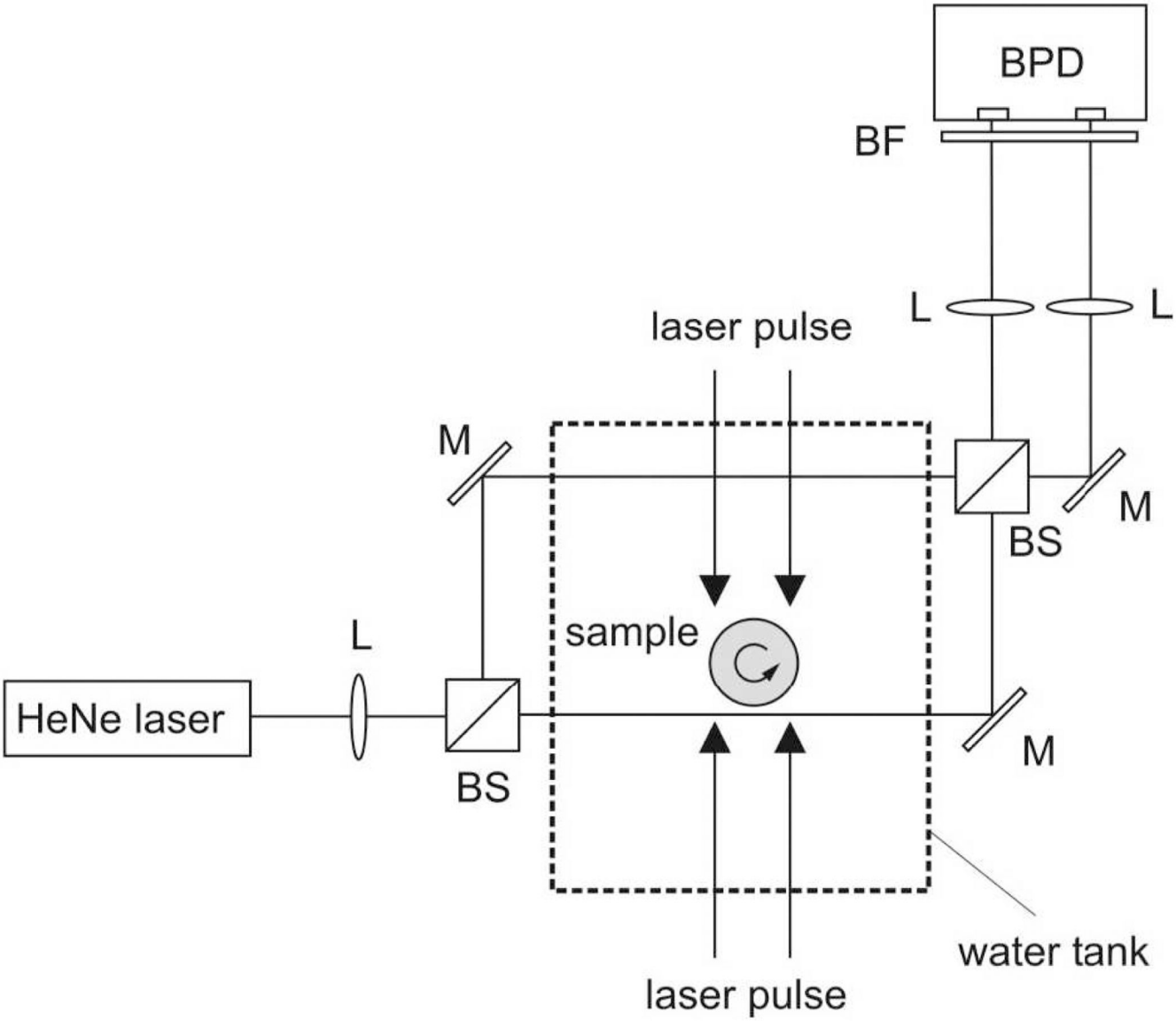

Figure 4.
Experimental setup for photoacoustic tomography with a Mach–Zehnder interferometer as acoustic line detector. BS, beam splitter; M, mirror; BPD, balanced photodetector; L, lens; BF, bandpass filter. Reprinted with permission from Ref. [62]

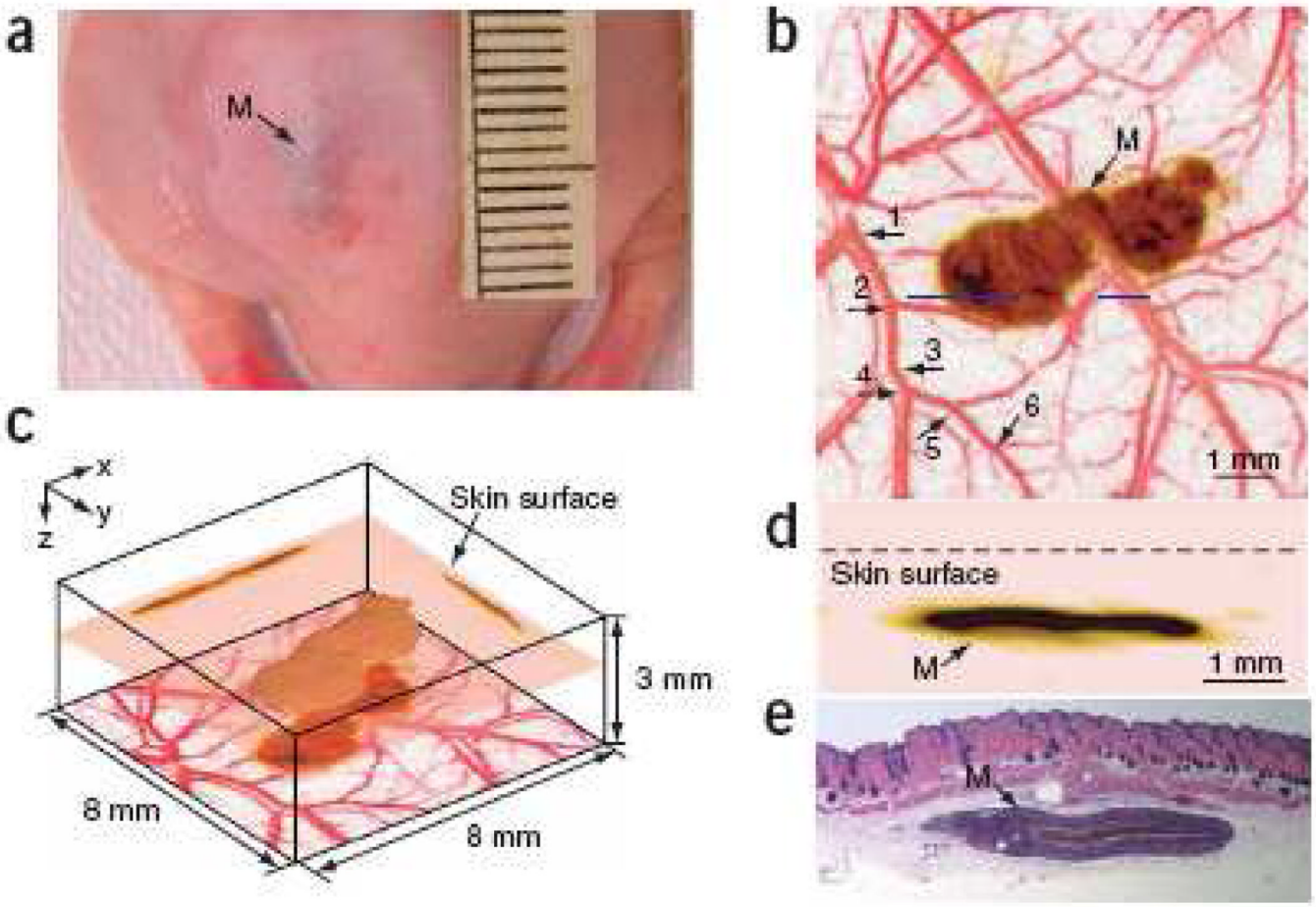

Figure 5.

(Color online) *In vivo* imaging of a subcutaneously inoculated B16-melanoma in an immunocompromised nude mouse using fPAM at 584 nm and 764 nm. (a) Photograph of the melanoma. (b) A composite of the two maximum amplitude projection (MAP) images projected along the z axis, where an MAP image is formed by projecting the maximum photoacoustic amplitudes along a direction to its orthogonal plane. Here, blood vessels are pseudocolored red in the 584-nm image and the melanoma is pseudo-colored brown in the 764-nm image. As many as six orders of vessel branching can be observed in the image, as indicated by numbers 1–6. (c) Three dimensional rendering of the melanoma from the data acquired at 764 nm. Two MAP images at this wavelength projected along the x and y axes are shown on the two side walls, respectively. The composite image shown in (a) is redrawn at the bottom. The top surface of the tumor is 0.32 mm below the skin surface, and the thickness of the melanoma is 0.3 mm. (d) An enlarged cross-sectional (B-scan) image of the melanoma parallel with the z-x plane at the location marked with a dashed line in (a). (e) Hematoxylin-and-eosin (HE) stained section at the same marked location. M, melanoma. Reprinted by permission from Macmillan Publishers Ltd: [Nature Biotechnology] [97], copyright (2006)

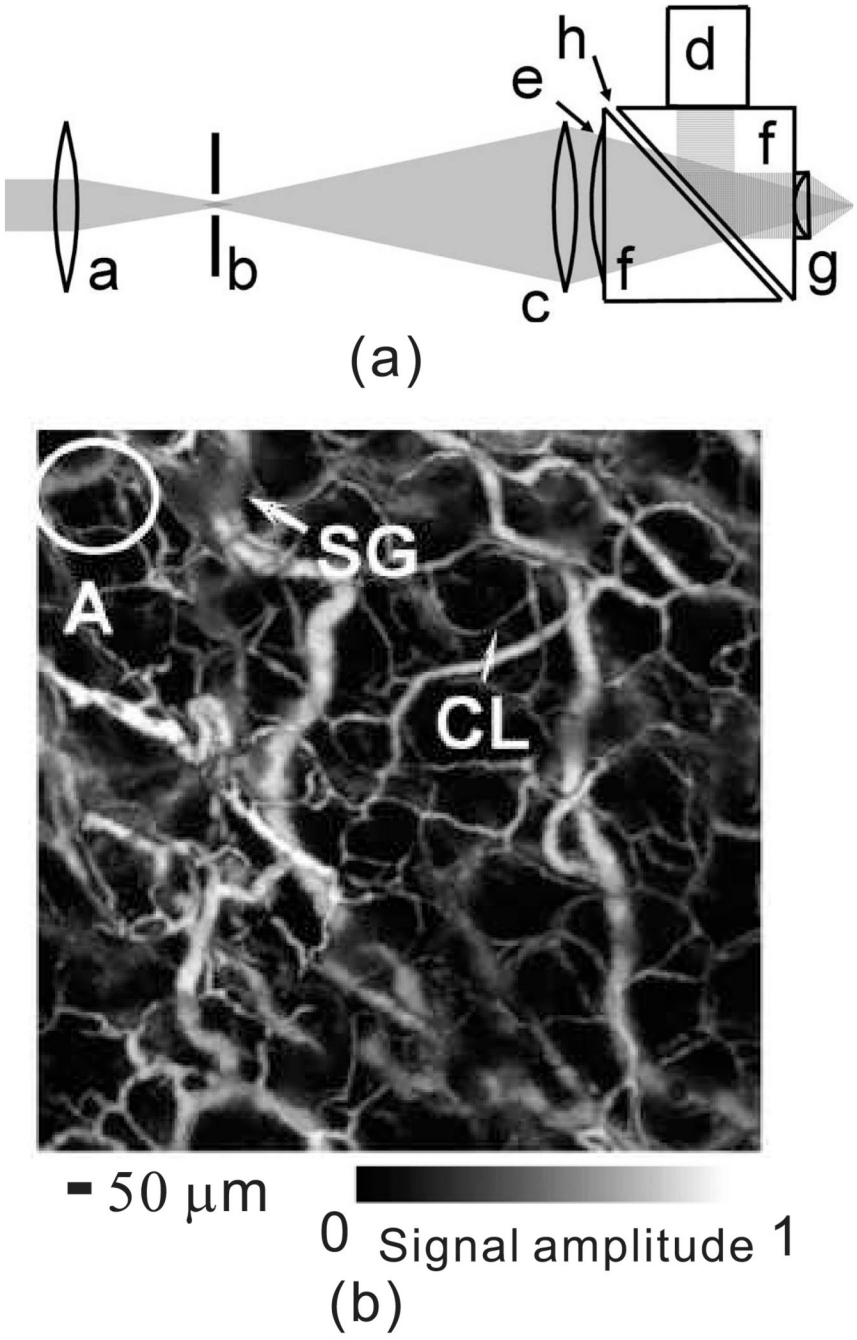

Figure 6.
(a) Schematic of the OR–PAM system. a, Condenser lens; b, pinhole; c, microscope objective; d, ultrasonic transducer; e, correcting lens; f, isosceles prism; g, acoustic lens; h, silicon oil. (b) *In vivo* OR–PAM image of microvasculature in a nude mouse ear. CL, capillary, and SG, sebaceous gland. Reprinted with permission from [99].

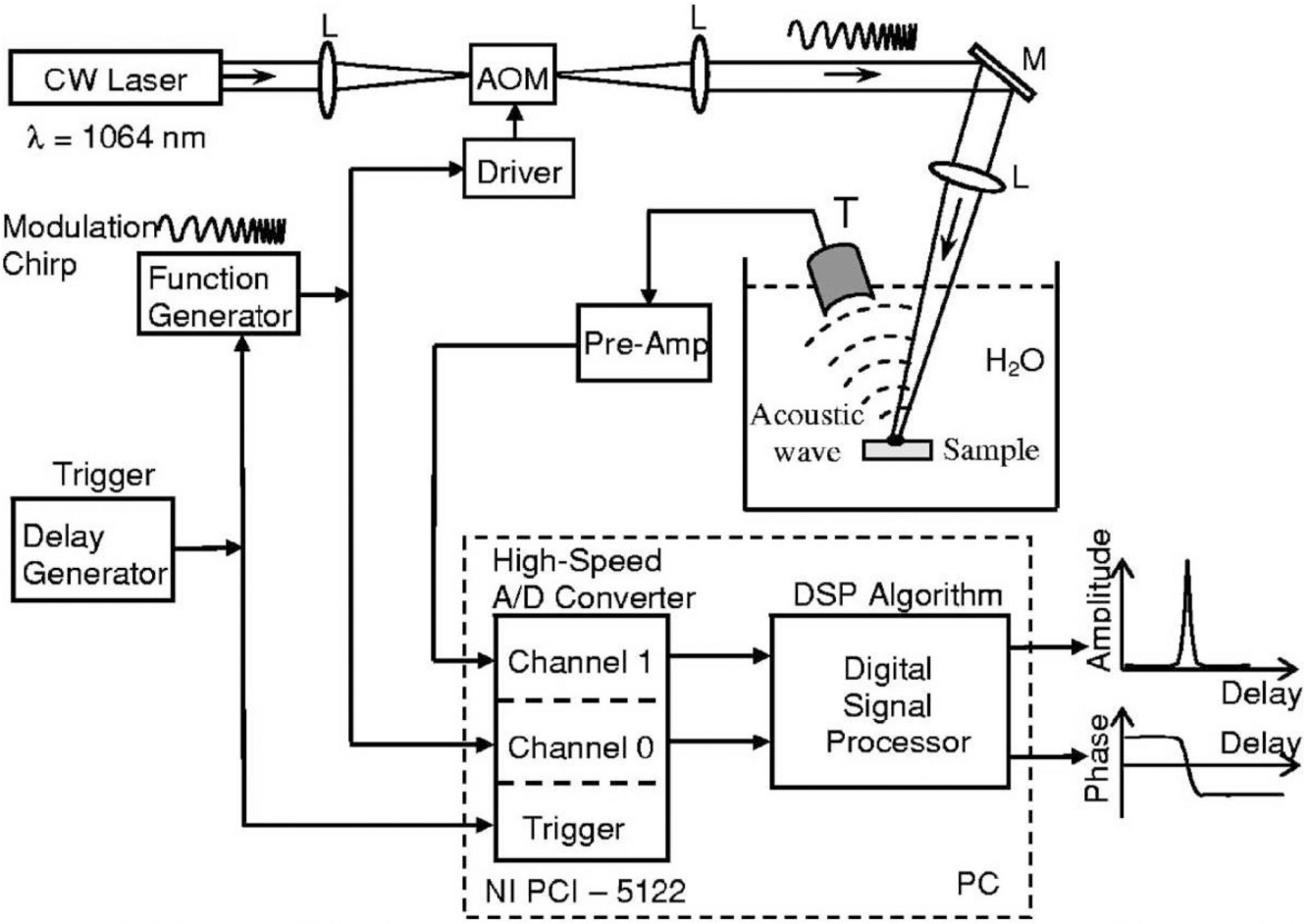

Figure 7.
Schematic diagram of the frequency-domain PA imaging system with a frequency-swept laser source. AOM–acousto-optic modulator, L–lenses, M–mirror, T–ultrasonic transducer. Reprinted with permission from [105].

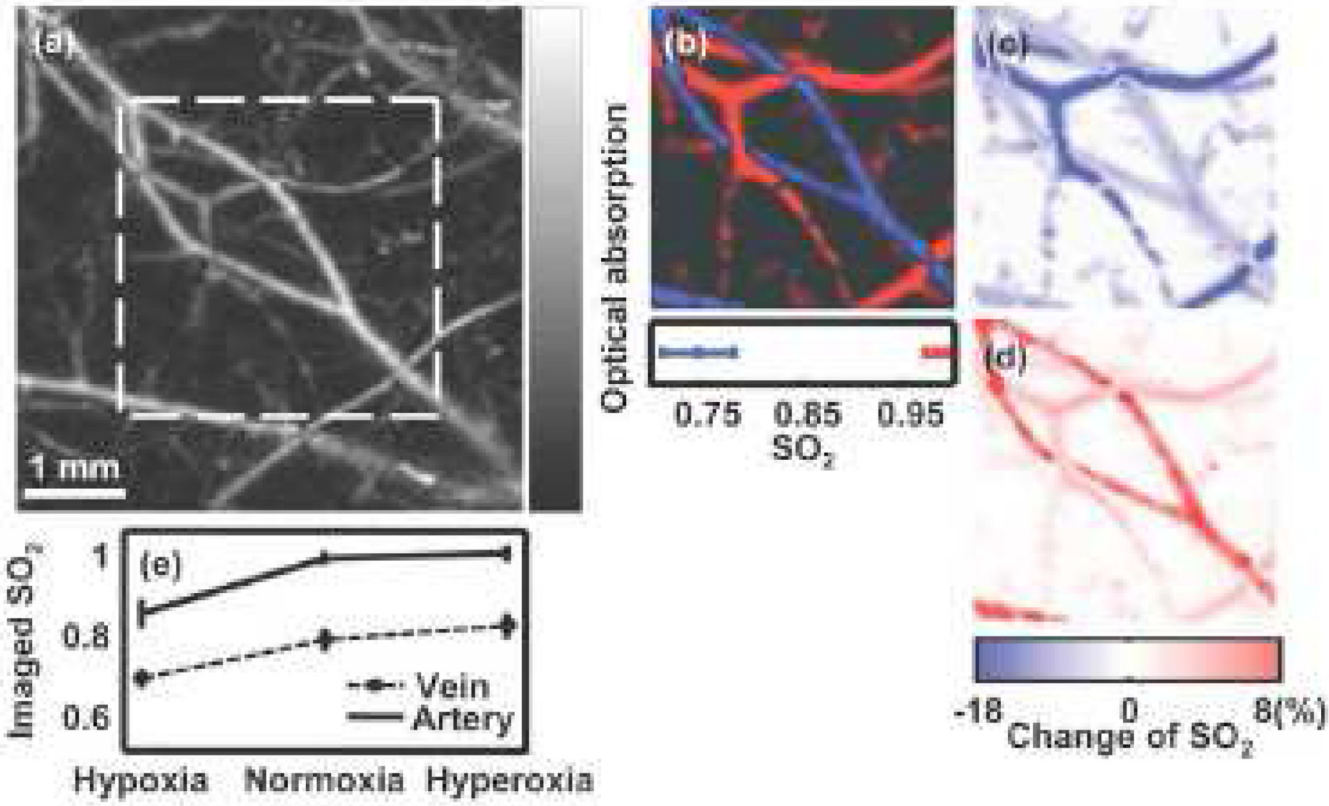

Figure 8.

(Color online) PAM imaging of variations in SO_2 in single subcutaneous blood vessels in a 200 g Sprague Dawley rat *in vivo*. (a) Structural image reflecting the total hemoglobin concentration acquired at the 584 nm optical wavelength under hyperoxia. (b) Static SO_2 image within the marked region in panel A under normoxia, where arteries and veins are pseudocolored red and blue, respectively, based on the imaged SO_2 values. (c) Image of the SO_2 changes from normoxia to hypoxia (hypoxia value-normoxia value). (d) Image of SO_2 changes from normoxia to hyperoxia (hyperoxia value-normoxia value). (e) Typical imaged values of SO_2 in venous and arterial bloods under all three physiological states, where different trends of variation are observed. [This results relies on invisive methods to measure local fluence rate]. Reprinted with permission from [109]. Copyright (2007), American Institute of Physics.

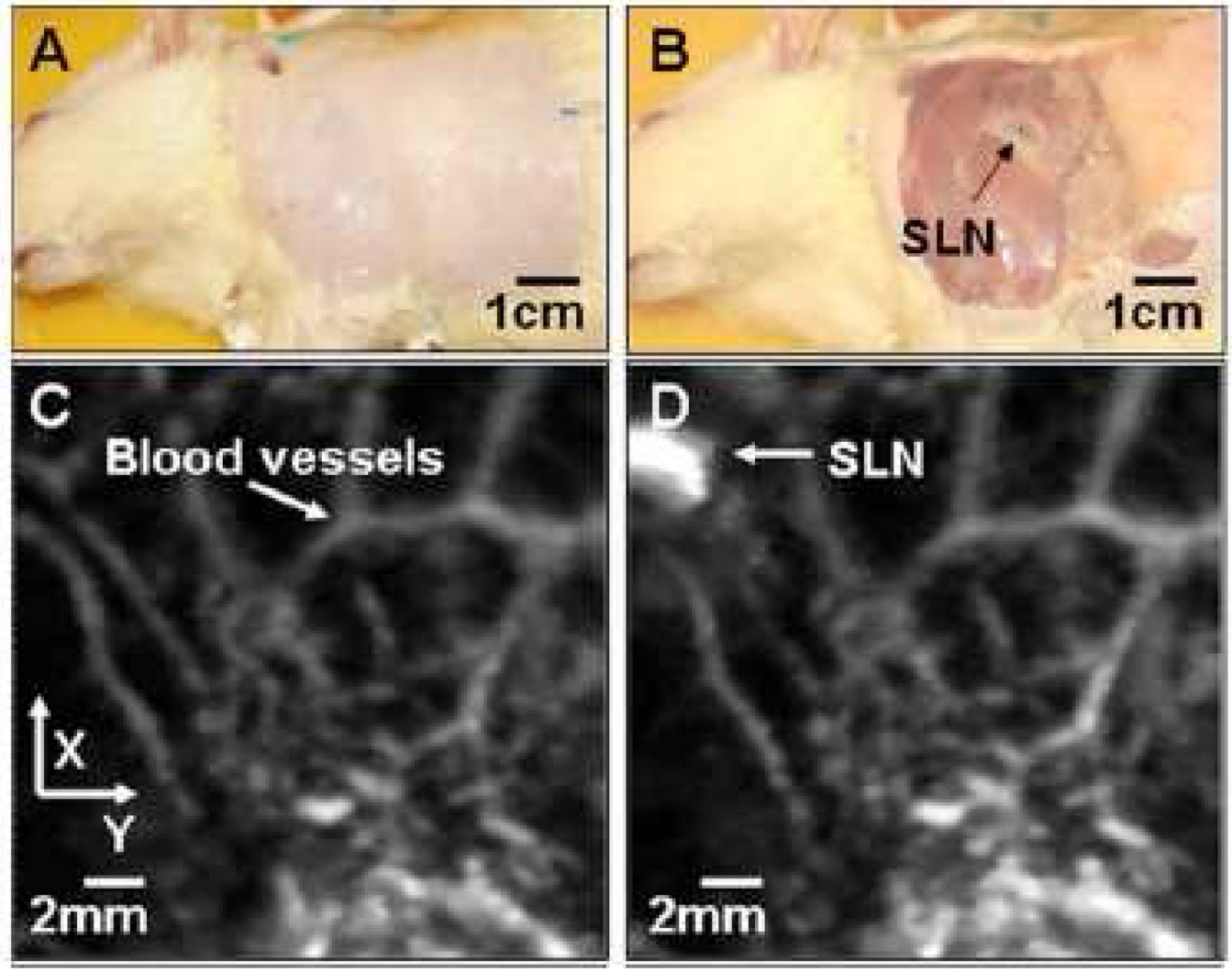

Figure 9.
(Color online) Noninvasive in vivo photoacoustic MAP images of the SLN in a rat. (A) Photograph with hair removed before photoacoustic imaging. (B) Photograph with skin removed after photoacoustic imaging. (C) Control photoacoustic image without methylene blue injection. Bright parts represent optical absorption, here, blood vessels. x and y denote B-scan and 3-D imaging. (D) After-injection photoacoustic image. Reprinted with permission from [127].

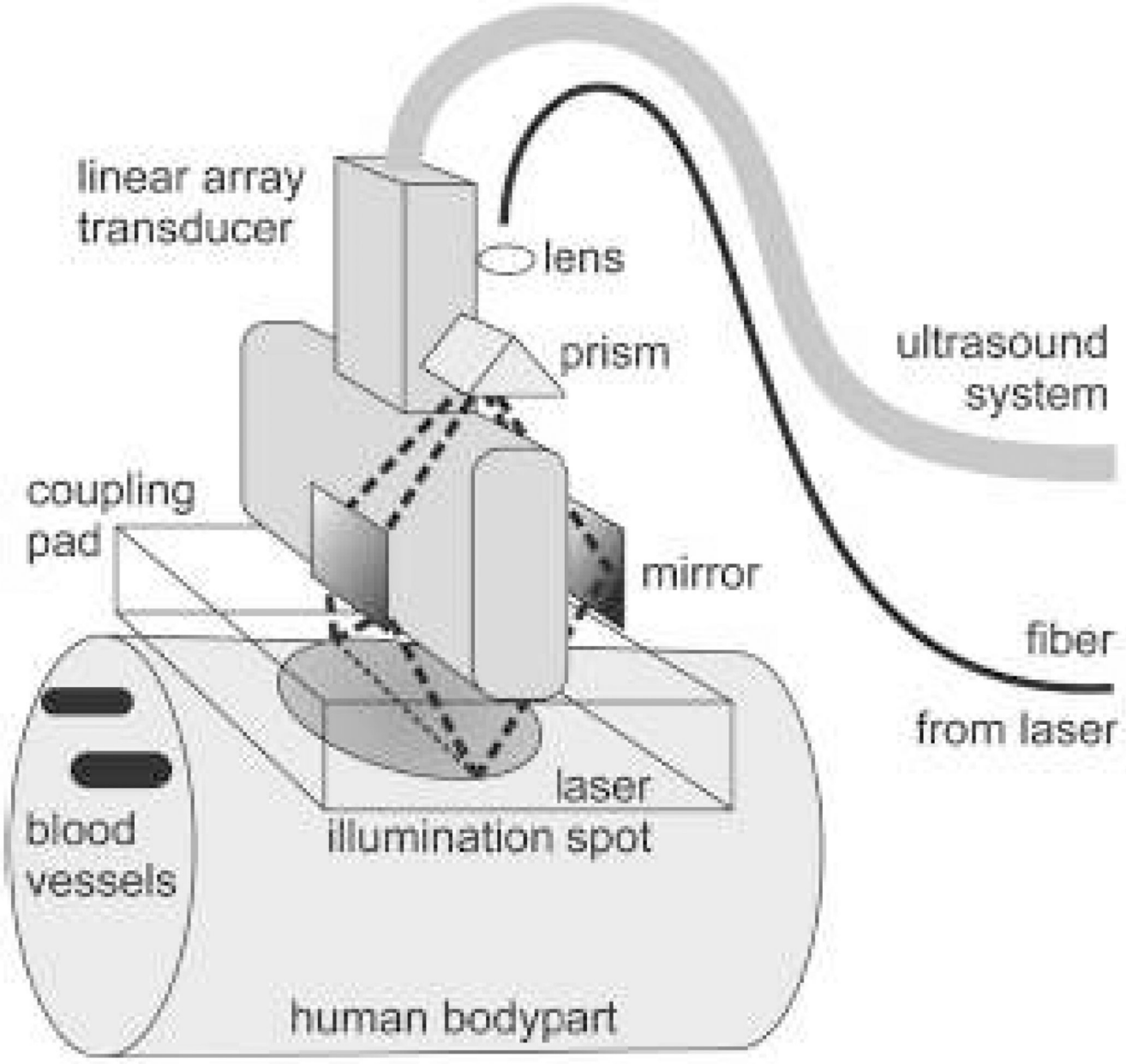

Figure 10.

Combined optoacoustic and ultrasound real-time imaging setup. Short laser pulses are delivered through a fiber to the illumination system consisting of a lens, a prism and two mirrors. The illumination system images the core of the fiber around the transducer onto a homogeneously illuminated spot on the skin. The light penetrates into the highly scattering tissue and is absorbed in blood vessels, resulting in ultrasound transient generation (thermoelastic effect). The ultrasound transients propagate back to the skin surface, through the transparent acoustic coupling pad onto the ultrasound transducer. The signals of 64 transducer elements are simultaneously recorded with an ultrasound system and passed onto a computer. The computer reconstructs an absorption distribution image and displays it on a screen with a repetition rate of 7.5 Hz. One single laser pulse is enough to get a complete image on the screen in less than 100-ms reconstruction time. Classical echo ultrasound images can

also be acquired for side by side comparison or for mixed mode imaging. Reprinted with permission from [65] (©2005 IEEE).

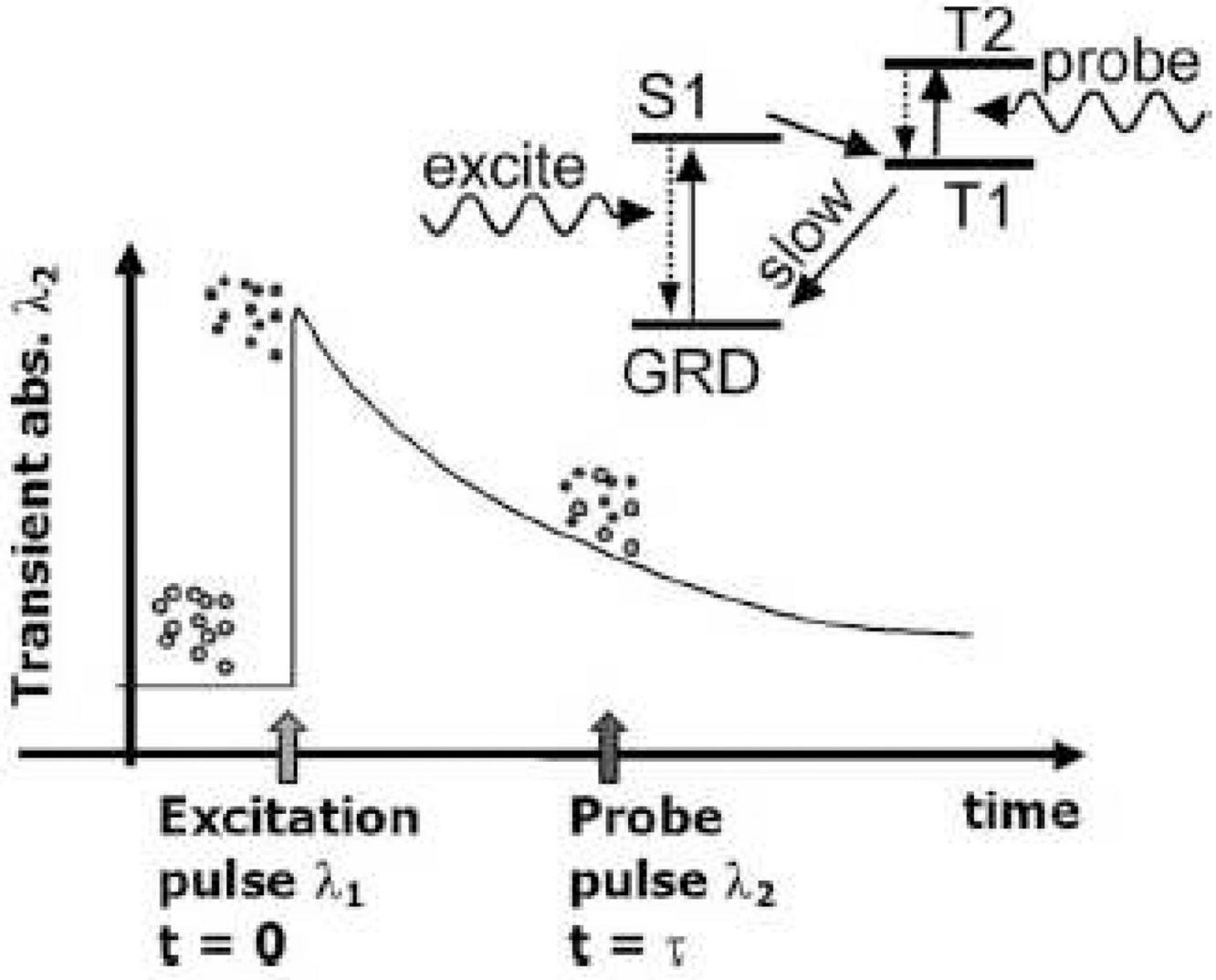

Figure 11.

Basic principle of photoacoustic lifetime measurement of a phosphorescent oxygen sensitive dye. Dye molecules at ground state (open circles) are excited at t=0 (closed circles) by a short laser pulse of wavelength λ_1 (532 nm in this paper). The dye molecule is excited to its first singlet state (S1) and then to a triplet state (T1) by internal system crossing. This process is relatively efficient (quantum yield of 50% for PtOEP dye) and occurs on a time scale of picoseconds. The population of the T1 excited state then decays back to the ground state via phosphorescence and quenching by collisions with oxygen molecules. The decay rate is relatively slow ~ 50 μs for PtOEP) and depends on oxygen concentration in the environment. A probe pulse (at 740 nm in this paper) fired at t=τ generates a photoacoustic response due to optical absorption corresponding to the T1 to T2 transition. The absorption is transient because of the decay of the population of the T1 state. The amplitude of the photoacoustic signal generated at different delay times τ is used to measure the decay rate of the T1 excited state population. Reprinted with permission from [146].

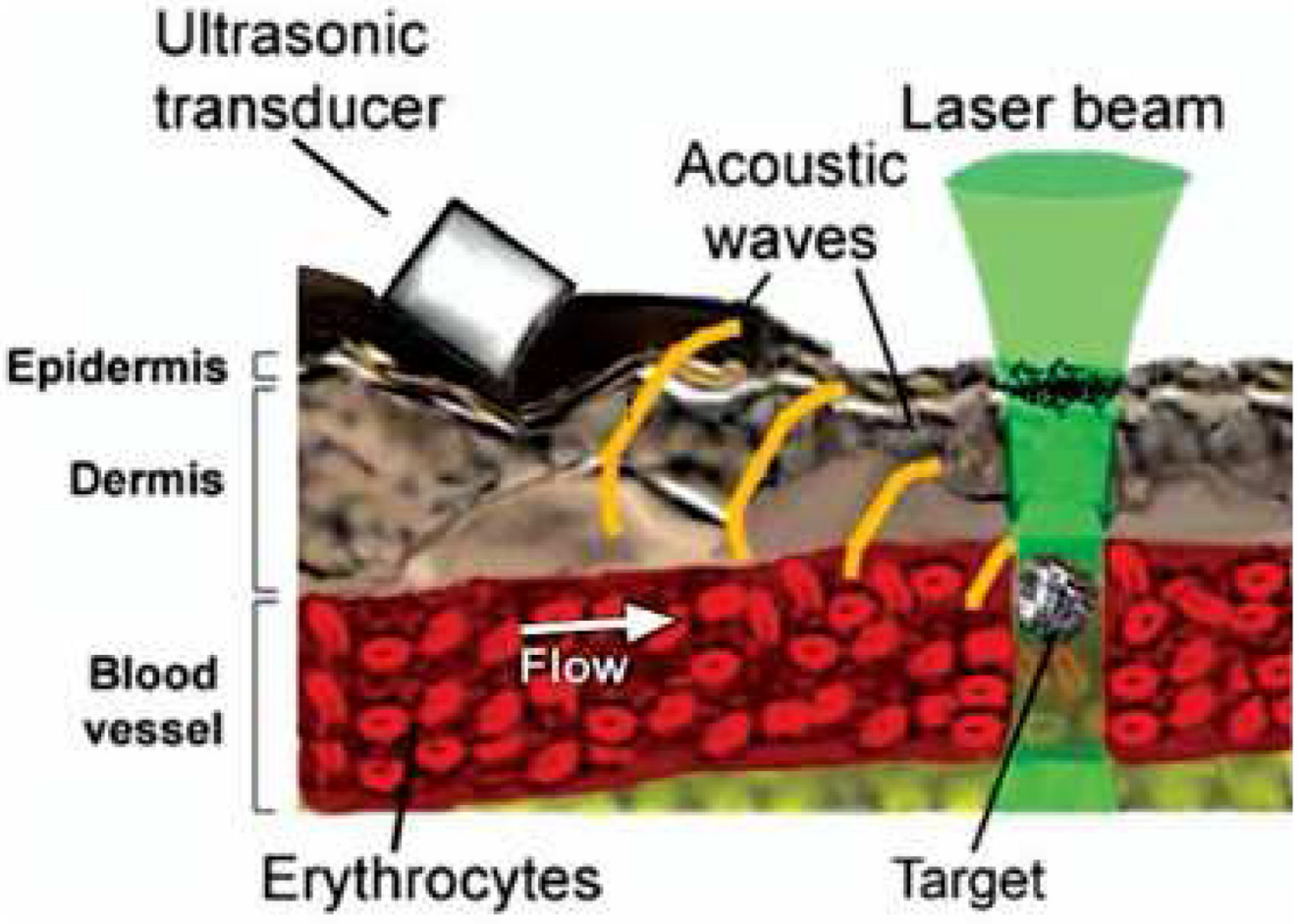

Figure 12.
(Color online) Principle of PA detection of single absorbing targets in blood flow *in vivo*. Reprinted with permission from [101].

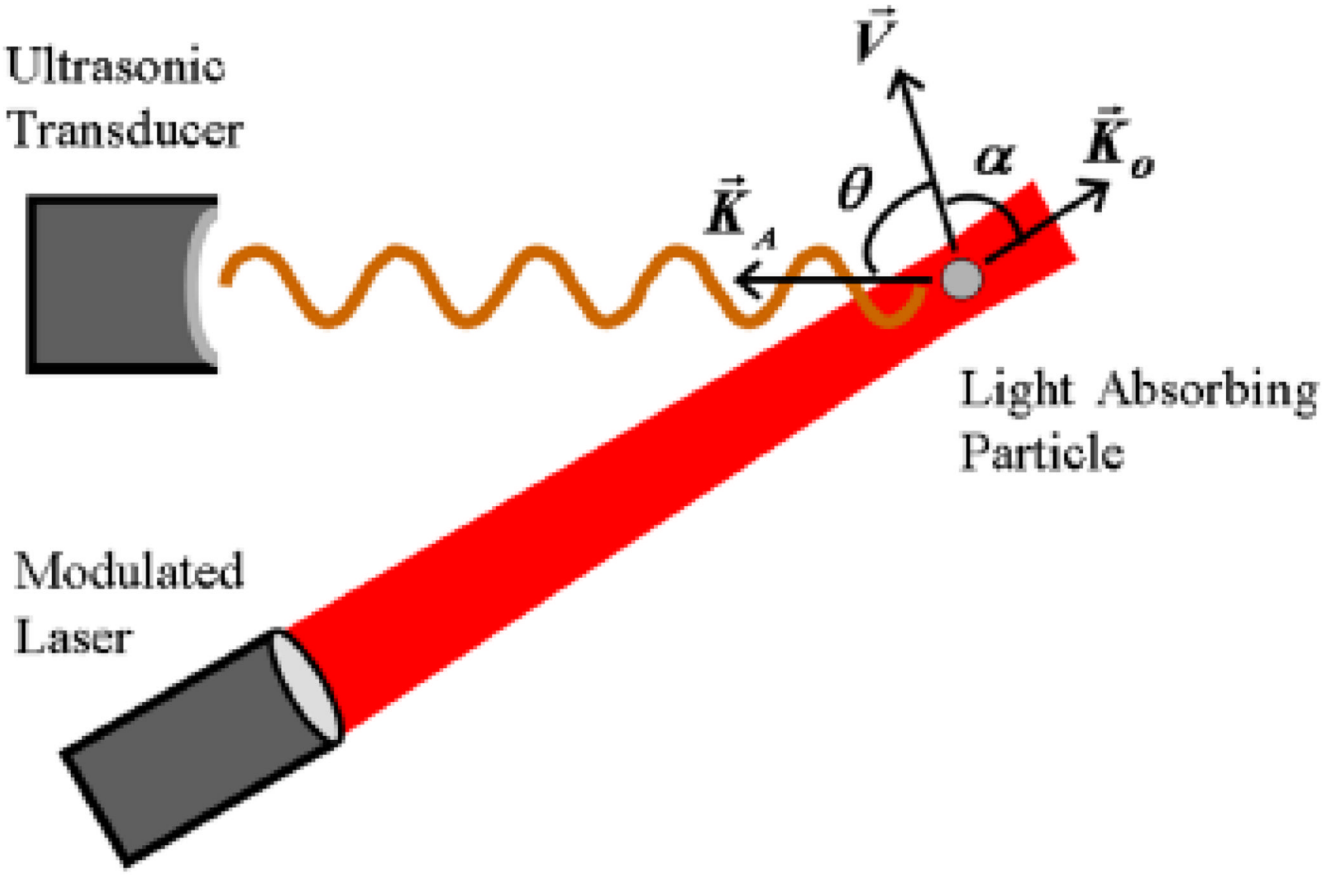

Figure 13.
(Color online) Schematic for photoacoustic Doppler shift. The small light–absorbing particle moving along the velocity vector is illuminated by modulated continuous–wave light. $\vec{K}_0$, $\vec{V}$ and $\vec{K}_A$ represent the directions of laser illumination, velocity of the absorber and acoustic waves, respectively. Reprinted figure with permission from [149]. Copyright (2007) by the American Physical Society.

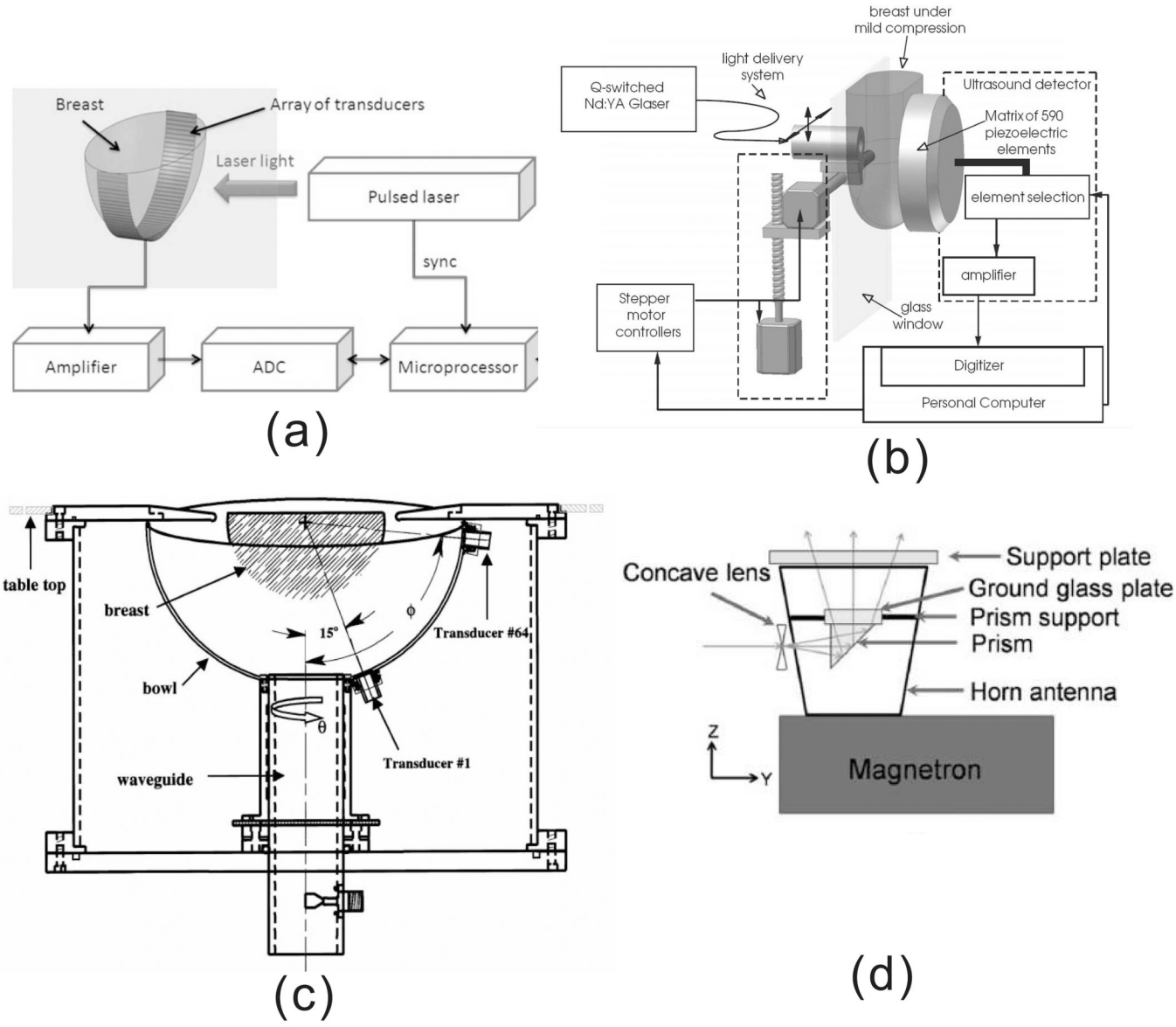

Figure 14.

Several designs of breast imaging systems based on the PA effect. (a) Schematic diagram of LOIS-64. [This system uses a 64-element arc array to detect the PA signal. The laser, at 757 nm wavelength, illuminates the breast from one side.] Reprinted with permission from [47]. (b) Schematic of the Photoacoustic Mammoscope. [This system used a 590-element ultrasonic transducer matrix to detect PA signals. The laser, at 1064 wavelength, illuminates the breast on the opposite side of the breast.] Reprinted with permission from [152]. (c) Schematic of thermoacoustic CT scanner for breast imaging. Sixty-four transducers are arrayed on a 0.18-inch- (0.5-cm)-thick, hemispheric, acrylonitrile-butadiene-styrene plastic bowl (14-inch [36-cm] diameter). The locations of the transducers are indexed by the angles u and f. Transducers 1 and 64 are shown. UHF energy at 434 MHz was provided by a 2.8-inch-(8-cm)-diameter, water-filled, cylindric wave guide. The imaging bowl is rotated about the wave guide by means of a belt drive and stepper motor (not shown). The imaging bowl and wave guide are filled with deionized water and placed inside a water-filled cylindric tank with a top coincident with

the top of the examination table. Reprinted with permission from [155]. (d) An integrated microwave horn antenna and optics. Reprinted with permission from [156].

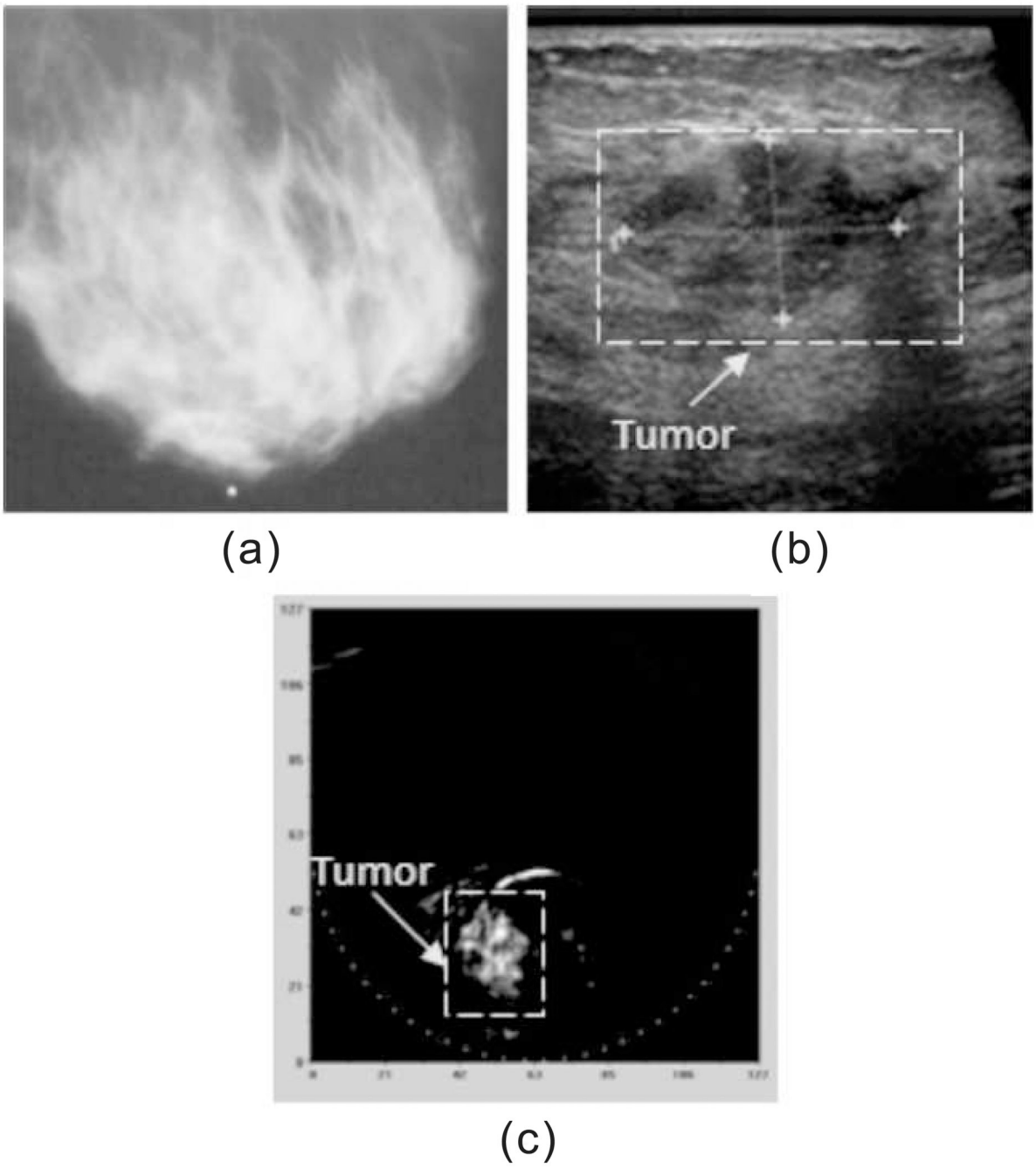

Figure 15.
Example of the clinical images showing the breast cancer: (a) mediolateral mammography, (b) ultrasonic, and (c) mediolateral optoacoustic images. High contrast of the object in the OA image implies the advanced angiogenesis indicative of a malignant tumor. Reprinted with permission from [47]

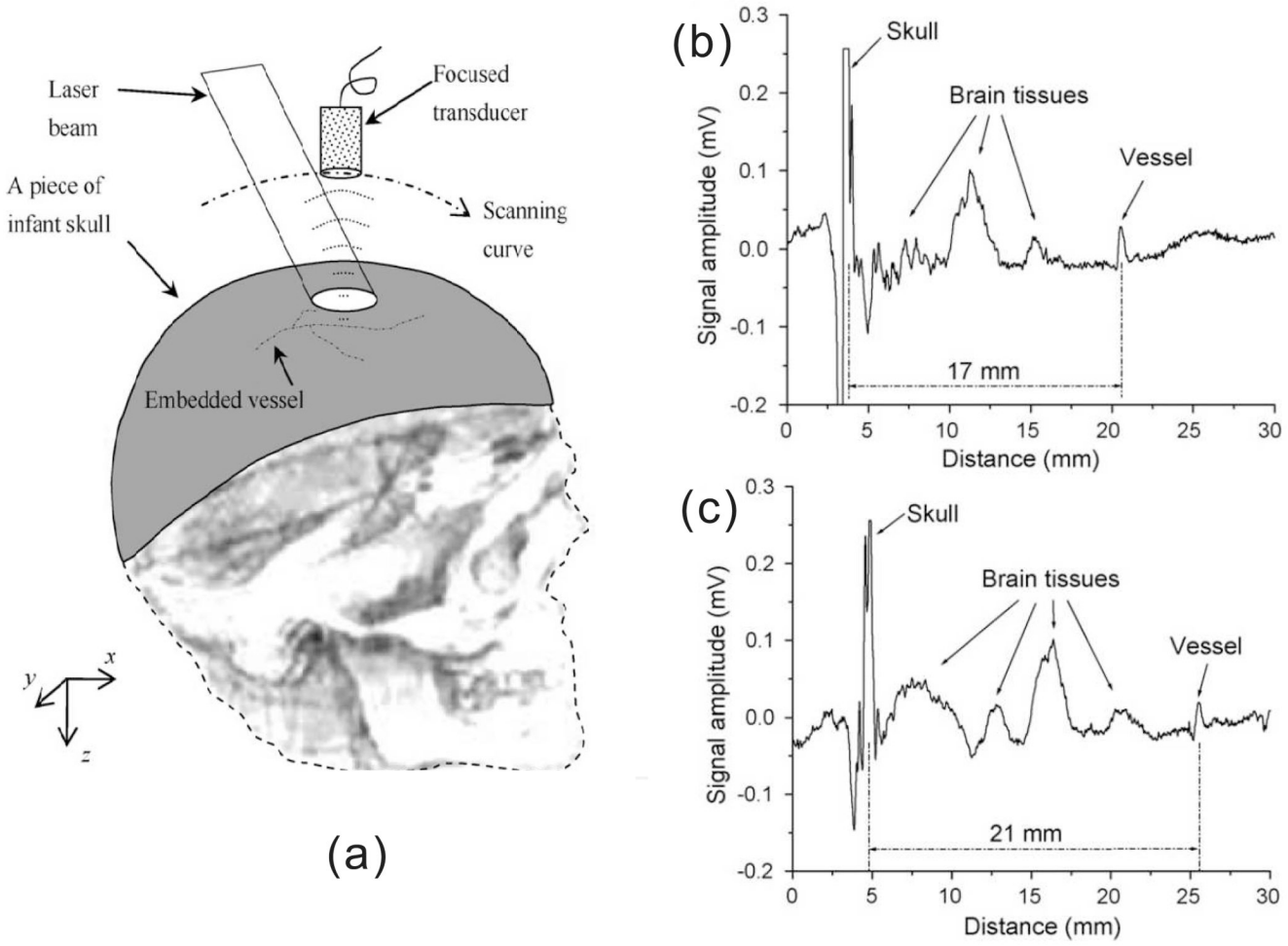

Figure 16.

(a) Geometry of reflection mode transcranial photoacoustic imaging of brain. (b) PA signals from a vessel embedded in fresh canine brain tissue beneath the infant skull. The distance between the vessel and the skull is 17mm. (c) PA signals from the same vessel at the distance of 21mm. Reprinted from [169], with permission from Elsevier.

Table 1

MPE for skin exposure to a laser beam at 400–1400 nm

Wavelength λ (nm)	MPE(1) (mJ/cm^2)	MPE(2) (mJ/cm^2)	MPE(3) (mW/cm^2)
400–700	20	$1100t^{0.25}$	200
700–1050	$20\times10^{2(\lambda-700)/1000}$	$1100\times10^{2(\lambda-700)/1000}t^{0.25}$	$200\times10^{2(\lambda-700)/1000}$
1050–1400	100	$5500t^{0.25}$	1000

Time t is in seconds

(1) 10^{-9}s ≤ t < 10^{-7}s;

(2) 10^{-7} s ≤ t<10 s;

(3) t >10 s.